CATÓLICA
FACULTY OF BIOTECHNOLOGY
PORTO

NANOTECHNOLOGICAL APPROACHES FOR TREATING SKIN CANCER: FROM DRUG DELIVERY NANOFORMULATIONS TO 3D MODELS OF SKIN CANCER

by

Marta Oliveira Vasconcelos Rosadas

September 2022

CATÓLICA
FACULTY OF BIOTECHNOLOGY
PORTO

NANOTECHNOLOGICAL APPROACHES FOR TREATING SKIN CANCER: FROM DRUG DELIVERY NANOFORMULATIONS TO 3D MODELS OF SKIN CANCER

A thesis presented to *Escola Superior de Biotecnologia* of the *Universidade Católica Portuguesa* to fulfill the requirements of a Master of Science degree in Biomedical Engineering

by

Marta Oliveira Vasconcelos Rosadas

Supervisor: Ph.D. Alessandra Quarta

Tutor (University): Ph.D. Ana Oliveira

September 2022

Abstract

Basal cell carcinoma is the most common skin cancer in the world. Even though its mortality rates are low, the number of cases has been rising worldwide. Photodynamic therapy mediated by 5-aminolevulinic acid (5-ALA) is a possible treatment for this kind of cancer. However, the penetration capability of 5-ALA into the deeper layers of the skin is limited, constraining the potential of this therapy.

To overcome this limitation, phosphocholine-based nanovesicles were developed, using a pH gradient active loading protocol, to serve as a drug delivery system and to improve the transdermal passage of 5-ALA. The vesicles were characterized by morphology, encapsulation efficiency, loading capacity, stability, and diffusion capacity using *ex-vivo* pig skin.

Additionally, a 3D cellular model was developed to resemble skin cancer, using a collagen hydrogel as a scaffold. Cellular tests were conducted using this skin model, which evaluated the vesicles' toxicity and penetration capability. Furthermore, preliminary tests of the efficacy of this therapy were carried out with 2D melanoma cells.

According to the results, with a feeding concentration of 833 µg/mL of 5-ALA, its encapsulation efficiency is 24%. The vesicles presented an average diameter of 154,8 ± 18,8 nm, which decreased slightly until day 15 of storage, from when the sample stabilized. The vesicles have good thermostability. The diffusion tests showed that the vesicles could penetrate the skin, therefore, have the potential as a transdermal drug delivery system.

Though the tumor target of this project is basal cell carcinoma, cellular tests have been performed with melanoma cells. The results show the therapeutic potential of the vesicles upon application of the photodynamic stimulus. In addition, preliminary studies with 3D hydrogel models of skin cancer embedded with melanoma spheroids and overlayed with keratinocytes demonstrate the capability of the vesicles to penetrate the matrix and enter the spheroids.

Keywords: nanovesicles; drug delivery systems; 5-aminolevulinic acid; 3D skin cancer models; skin cancer therapies; photodynamic therapy

Resumo

O carcinoma basocelular é o cancro de pele mais comum no mundo. Embora apresente baixas taxas de mortalidade, o número de casos tem vindo a aumentar em todo o mundo. A terapia fotodinâmica mediada por ácido 5-aminolevulínico (5-ALA) é um possível tratamento para este tipo de cancro. Porém, a capacidade de penetração do 5-ALA nas camadas mais profundas da pele é limitada, comprometendo o seu potencial.

Para superar essa limitação, neste trabalho, nanovesículas à base de fosfocolina foram desenvolvidas, usando um protocolo de encapsulamento ativo por gradiente de pH, que servirão como um sistema de libertação controlada de fármacos, facilitando a passagem transdérmica de 5-ALA. Estas foram caracterizadas quanto à sua morfologia, eficiência do encapsulamento, capacidade de carga, estabilidade e capacidade de difusão.

Adicionalmente, um modelo celular 3D foi desenvolvido para representar cancro da pele, utilizando um hidrogel de colagénio-agarose como *scaffold*. Através de testes celulares neste modelo, avaliaram-se a toxicidade e capacidade de penetração das nanoparticulas. Adicionalmente, testes preliminares da eficácia desta terapia foram realizados com culturas 2D de células de melanoma.

De acordo com os resultados, para uma concentração inicial de 5-ALA de 833 μg/mL, a eficiência de encapsulamento obtida foi de 24%. As nanovesículas apresentaram diâmetro médio de 154,8 ± 18,8 nm, que diminuiu ligeiramente até o 15º dia de armazenamento, a partir do qual a amostra estabilizou. As vesículas apresentaram boa estabilidade térmica. Os testes de difusão mostraram que as vesículas foram capazes de penetrar a pele.

Embora a patologia alvo deste projeto seja o carcinoma basocelular, os testes celulares foram realizados com células de melanoma. Os resultados mostraram o potencial terapêutico das vesículas mediante aplicação de estímulo fotodinâmico. Além disso, estudos preliminares com o modelo 3D desenvolvido demonstram a capacidade das vesículas de penetrar na matriz do hidrogel e entrar nos esferoides.

Palavras-chave: nanovesículas; sistemas de libertação controlada; ácido 5-aminolevulínico; modelo 3D de cancro da pele; terapias para cancro da pele; terapia fotodinâmica

Acknowledgments

Firstly, I would like to express my gratitude to my supervisors, whom I admire very much. Ph.D. Alessandra Quarta, for all the guidance, patience, and knowledge you passed on to me, Ph.D. Clara Piccirillo for welcoming me to Italy and for all the advice and help inside and outside the CNR, and Ph.D. Antonio Gaballo for his wise advice and the support he gave to improve my work

To all the people I met in the CNR Nanotec and to my lab colleague, Giorgia Riccardo, I'd like to thank you for always making me feel so welcomed and for your generous help during the time I spent there.

To the friends I made in Lecce, thank you for the moments we shared and your support in my work.

A big thanks to my friends from college for making this journey easier and more fun. A special thanks to my friend Helena Costa, who walked alongside me during these years and shared the Erasmus experience with me. It wouldn't be so great without you.

To my hometown friends, a huge thanks for your friendship and support. I consider myself very lucky to have you as my friends.

To my family, in particular, my parents, sister, and grandparents, thank you for all the opportunities you have given me, the love and care, and for always believing in me. To my dog, thank you for your emotional support.

Finally, a very special thanks to my mother for constantly pushing me to do more and better and for making everything possible.

Thank you all!

Contents

List of Figures

List of Tables

List of abbreviations

2D – Two-dimensional

3D – Three-dimensional

5-ALA – 5-Aminolevulinic acid

ALA INV – Invasomes loaded with 5-ALA

BCA – Bicinchoninic acid assay

BCC – Basal cell carcinoma

CisPC – 1,2-dioleoyl-sn-glycero-3-

DCF – 2',7'-dichlorofluorescein

DCFH – 2',7'- dichlorodihydrofluorescein

DCFH-DA – 2',7'- dichlorofluorescein diacetate

DLPC 12 – 1,2-dilauroyl-sn-glycero-3-phosphocholine, 12 carbons alkyl chain

DLPC 14 – 1,2-dilauroyl-sn-glycero-3-phosphocholine, 14 carbons alkyl chain

DLS – Dynamic light scattering

DMEM – Dulbecco's Modified Eagle Medium

DMPC – 1,2-dimyristoyl-sn-glycero-3-phosphocholine

DMSO – Dimethylsulfoxide

DSPE – 1,2-Distearoyl-sn-glycero-3-phosphorylethanolamine

DTG – Differential thermogravimetric

ECM – Extracellular matrix

EE – Encapsulation efficiency

Empty INV – Empty Invasomes

FBS – Fetal bovine serum

FDA – Food and Drug Administration

HaCaT – Human keratinocytes cell line

HBL – Human melanoma cell line (HBL)

LC – Loading capacity

Lecithin – L-α-lyso-Lecithin, from Egg Yolk

MCF7 – Michigan Cancer Foundation-7

MTT – 3- [4,5-dimethylthiazol-2-yl] -2,5-diphenyl tetrazolium bromide

NAD – Nicotinamide adenine dinucleotide

NPs – Nanoparticles

O.N. – Overnight

PBS – Phosphate Buffered Saline

PDI – Polydispersity index

PDT – Photodynamic therapy

PpIX – Protoporphyrin IX

RHOD INV – Invasomes loaded with Rhodamine

RIPA – Radioimmunoprecipitation assay

ROS – Reactive oxygen species

RPMI – Roswell Park Memorial Institute

RT – Room temperature

SC – Stratum corneum

SDH – Succinate dehydrogenase

TE354.T – Human basal carcinoma cell line

TEM – Transmission electron microscopy

TGA – Thermogravimetric analysis

ZP – Zeta potential

1. Introduction

1.1 Skin

It is already a well-known fact that the skin is the largest organ in the human body, representing around 15% of the total body weight of an adult. It is in charge of critical vital functions such as protection against physical, chemical, and biological hazards, regulation of the water loss from the body, thermoregulation, and getting sensory information about its environment (Kolarsick, et al., 2011). It comprises two main layers, the epidermis and the dermis.

The epidermis, the outermost layer, is mainly composed of proliferating and differentiating keratinocytes, cells responsible for producing a long threadlike protein with a protective function called keratin. In the deepest part of the epidermis, the *stratum basale*, a layer usually one cell thick, keratinocytes proliferate through mitosis and emerge to the upper layers passing through stratum spinosum, stratum granulosum, until the *stratum corneum* (SC). Along these layers, cells suffer a differentiation process called keratinization. By the time they reach the SC, they have lost their nuclei and cytoplasmic organelles, have a flat appearance, and the keratin filaments align into cross-linked macrofibres. When they reach the skin's surface, they are shed, a process named desquamation (Kolarsick, et al., 2011) (Venus, et al., 2010).

The time from cell division to shedding is around 28 days long but can be altered in case of some diseases. For example, DNA damage caused by carcinogenic agents may mutate cell proliferation and affect the rate of cell division (Kolarsick, et al., 2011) (Venus, et al., 2010).

Connected to the epidermis by the basement membrane is the second layer of the skin, the dermis. It is mainly composed of a structural protein named collagen, which forms an extracellular matrix with molecules of elastic fibers and hyaluronic acid. Its primary function is to provide tensile strength and elasticity, offering protection from stress and strain. The hair follicles, sebaceous glands, apocrine glands, sweat glands, and blood and lymphatic vessels are in this layer. It is also here that it is possible to find the nerve endings that give us the sense of touch and heat.

Bellow the dermis, there is the subcutaneous tissue or hypodermis. It is mainly made of fibroblasts, adipocytes, and macrophages. Its functions include supplying the skin with blood and nerve vessels and providing cushioning and thermic isolation to the body.

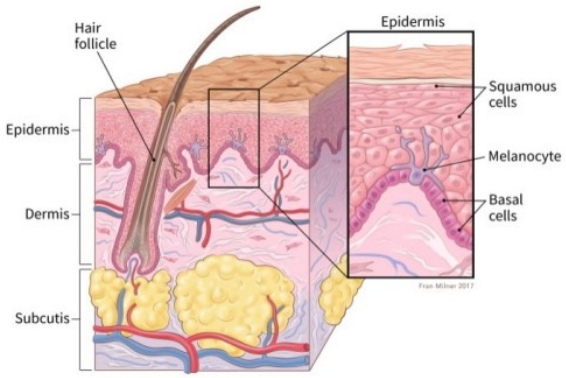

Figure 1.1 - Scheme of the anatomy of the skin

1.2 Basal Cell Carcinoma

Basal cell carcinoma (BCC) is a malignant tumor generated from the basal cells of the epidermis. It is the most common type of skin cancer, accounting for 80% of nonmelanoma cancers, but it also has higher survival rates (Matei, et al., 2013) (Dika, et al., 2020). Each year more than 1 million cases are reported in the United States, and in Europe the number of cases observed increased by 5% in the past ten years (Dika, et al., 2020). Australia stands on the podium for the highest incidence of BCC (Rubin, et al., 2015) (Peris, et al., 2019). The rise in BCC rates has been reported to be a result of the increasing longevity of the population, sun exposure behaviors, and the increase in diagnosis (Peris, et al., 2019).

The risk factors for developing this kind of cancer can result in the interaction between environmental and genetic factors. Exposure to UV light is the primary factor, especially acute intermittent exposure during childhood and teenage years is linked to a higher risk of having it during the lifetime (Dika, et al., 2020) (Rubin, et al., 2015). Regarding genetic risk factors, people who suffer from some hereditary diseases are much more likely to have BCC. The Gorlin syndrome is one of the most usual autosomal dominant genodermatoses, characterized by multiple BCC development. Other hereditary disorders predisposing to BCC are Xeroderma Pigmentosum and Bazex syndrome (Dika, et al., 2020).

1.3 Basal Cell Carcinoma treatments

Given the low metastatic rates, the treatment for BCC focus on local control. Treatments can be divided into surgical and nonsurgical. The choice of which one to apply

depends on the type of BCC, its size, location, the definition of its margins and the patient's comorbidities.

Surgical approaches include curettage and desiccation, cryosurgery, surgical excision, and Mohs surgery. These procedures have five-year cure rates of at least 95% for low-risk tumors (Rubin, et al., 2015).

Nonsurgical approaches encompass radiotherapy, topical and injectable therapy, and photodynamic therapy. These can be applied alone or in combination with each other.

1.4 Photodynamic Therapy

Photodynamic therapy (PDT) is a medical treatment based on activating a photosensitizer by light. A photosensitizer, which can be of exogenous or endogenous origin, can selectively concentrate around malignant tissue. When irradiated by light with a specific wavelength, it is catalyzed into reactive oxygen species (ROS). These molecules damage biomolecules such as proteins and lipids, destroying the tumor cells by necrosis and apoptosis (Malik, 2020). The primary step in PDT is the administration of the photosensitizer by either oral, venous, or topical application. The time it takes to reach and accumulate in the target tissues is called lag time, after which a light beam is applied in the desired area, activating it (Traylor, et al., 2021) (Matei, et al., 2013).

PDT was introduced in the 20th century, and its clinical applications have grown broadly, being an approved procedure for producing selective cytotoxicity in neoplastic tissues. Today it is most commonly used in treating dermatological conditions and has shown success in treating squamous cell carcinoma and BCC (Peris, et al., 2019) (Traylor, et al., 2021).

As a treatment for BCC, PDT has shown to be efficient, with 79 to 100% of complete response rates. In turn, the recurrence rates range from 6 to 44%, decreasing with multiple treatments, which seems to be the biggest stumbling block of this method (Rubin, et al., 2015). This treatment is typically considered for low-risk and superficial nodular types when surgery is unsuitable due to patient-related constraints. Compared with the other existent therapies that can cause complications such as pain, disfigurement, edema, secondary infection, hypopigmentation, scarring, and radiodermatitis, PDT shows shallow side effects, and the esthetic results are very superior (Peris, et al., 2019) (Krishnan & Mitragotri, 2020).

Regarding photosensitizers, most studies conducted up to the moment focus on protoporphyrin IX (PpIX) precursors, particularly 5-ALA and its methylated ester form, methyl amino levulinate (Matei, et al., 2013).

1.5 5-Aminolevulinic acid and its use as a Photodynamic Therapy mediator

5-Aminolevulinic acid (5-ALA) is a stable small non-proteinogenic amino acid, precursor of Heme biosynthesis. In cells, during the Heme synthesis pathway, this molecule is converted into PpIX, a photosensitizer. When 5-ALA is administrated exogenously is observed some additional free PpIX. It was reported in the 1950s that human volunteers orally consumed a 5-ALA solution resulting in a phototoxic skin reaction that was exacerbated with sunlight exposure (Traylor, et al., 2021) (Thunshelle, et al., 2016).

After its discovery, it was tested, and its potential as a diagnosis and treatment tool for cancer was revealed, being 1998 the year that its sensitivity and specificity for detecting malignant tissue were reported for the first time by Stummer, W. *et al.* (Traylor, et al., 2021) (Stummer, et al., 1998). 5-ALA was clinically shown to have intracellular tumor-specific fluorescence, making it helpful for intraoperative visualization of malignant issues in various organ systems. It has clinical evidence from dermatology, gynecology, urology, cardiothoracic and gastrointestinal surgery (Malik, 2020).

Further attractive proprieties are attributed to 5-ALA, such as its fast elimination inside the body, it is readily bioavailable after its administration in oral formulations, the fact that it accumulates in not many nonmalignant tissues (for instance, the gastrointestinal mucosa, salivary gland, bile ducts, and seminal vesicles) providing a good signal without much noise for tumor imagining, and as it is an endogenous human metabolite its usage is not accompanied by toxic side effects (Traylor, et al., 2021).

Considering these findings, in 2007, the European Medicines Agency approved the use of 5-ALA. In turn, the United States Food and Drug Administration's (FDA) approval took longer, being authorized only in 2017 the use of 5-ALA for glioma fluorescence imaging during surgery (Traylor, et al., 2021) (Malik, 2020).

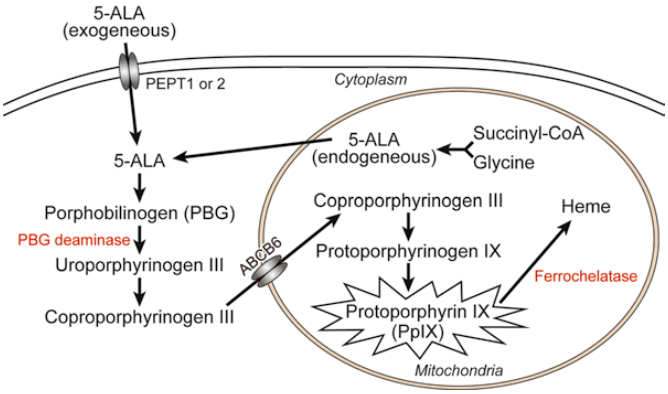

Figure 1.2 - Uptake of 5-ALA inside the cell and biosynthesis of PpIX

The main limiting characteristic of 5-ALA is its poor permeability through the skin. As this molecule is hydrophilic and the *stratum corneum* is very hydrophobic, it makes the passage of the drug problematic. Nanotechnology has developed solutions to overcome this, which is the greatest barrier against transcutaneous drug delivery and potentiate 5-ALA and other drugs' entrance into the skin (Thunshelle, et al., 2016).

1.6 Nanotechnology and drug delivery

Nanotechnology is a realm of science that uses techniques, materials, and equipment that operate at the nanoscale (1-1000 nm) (Dianzani, et al., 2014). It has been providing solutions for many problems, including the development of drug delivery systems. The creation and improvement of solutions for diagnosing, treating, and preventing diseases using nanotechnology is related to a more specific field of research called nanomedicine. Nanotechnology and nanomedicine research and investment have grown significantly. In two decades of research, according to Patra J. *et al.*, around 1500 patents have been published, several clinical trials have been carried out, and 51 products are currently being applied in clinical practice, with cancer diagnosis and treatment being the most popular theme (Patra, et al., 2018). All the solutions this field encompasses have the same raw material – nanoparticles.

Nanoparticles consist of materials designed at an atomic or molecular level that have the capacity to move through our body and interact with it. These can be made from polymers, metals, organic or inorganic molecules, dendrimers, and lipids. Its characteristics can also be designed according to its final purpose since its efficiency depends on its size, shape, and other physical and chemical properties.

Drug delivery systems are a group of technologies that regulate the delivery and release of pharmacologically active substances into the target tissue cells. These systems increase the drug's selectivity, bioavailability, and control of its release, maximizing its therapeutic effects and minimizing possible side effects. There are plenty vias of administration, such as oral, transdermal, lung inhalation, through the mucosa, and intravenous injection (Jeong, et al., 2021).

As drug delivery systems, nanoparticles present several benefits. Among them, the capacity to stay in the circulatory system and extend the drug's half-life, the ability to penetrate inside cells, and the possibility of targeting specific cells without damaging the healthy ones (Jeong, et al., 2021). Predictably, this promising topic will remain a big theme for research and development in the future decades (Patra, et al., 2018) (García-Pinel, et al., 2019).

Relatively to the nanoparticles' ways of achieving nanocarrier tissue targeting, there are two main ways: passive and active targeting (García-Pinel, et al., 2019). Passive targeting occurs when the nanoparticles enter the tumor cells by molecular movement through the cell membrane, as happens with liposomes. In turn, the active targeting is achieved by modifying the structure of the nanoparticles by adding, for example, antibodies that recognize the tumor (Patra, et al., 2018). A third way of targeting is the possibility of making nanoparticles stimulus-sensitive, making them alter themselves when facing an external trigger, such as a pH, temperature, or magnetic change (Patra, et al., 2018). Nanoparticles also benefit from the enhanced permeability and retention (EPR) effect, which was described in 1986 by Hiroshi Maeda and colleagues, consisting of the exceptional pathophysiological phenomenon of tumor vascularization (Wu, 2021) (Danaei, et al., 2018). It remains a controversial topic, but according to it, tumor vessels are highly permeable to macromolecules (including nanoparticles) and tend to accumulate them more in the tumor tissue than in the normal healthy tissue.

1.7 Nanoparticles for dermal delivery

Compared to the other vias of administration, such as intravenous and oral, dermal delivery is noninvasive and has significantly fewer side effects. Furthermore, since it doesn't involve passage through the digestive system, there's no loss due to first-pass metabolism (Jeong, et al., 2021). These benefits make it a very attractive solution for the prevention and treatment of many diseases, such as cancer (Krishnan & Mitragotri, 2020).

The biggest issue in this delivery type is the SC passage. Some systems have already been developed to help overcome this barrier, such as ionophoresis, sonophoresis, electroporation, micro-needling, and thermal ablation (Jeong, et al., 2021) (Krishnan & Mitragotri, 2020). Moreover, the use of nanoparticles for dermal delivery is a solution that has received considerable interest, adding to all the advantages that the use of nanoparticles offers to drug delivery, when their design and engineering are done optimally, they can make skin crossing possible (Jiang, et al., 2020) (Krishnan & Mitragotri, 2020).

Depending on its purpose, nanoparticles can be retained on the skin surface, penetrate through the skin, accumulate on the deeper layers, or infiltrate until they reach the bloodstream entering the systemic circulation. When dermal absorption is needed, depending on the particle's physicochemical characteristics, it can occur through different routes: the trans-appendageal route, the intercellular route, and the transcellular route (Figure 1.3) (Krishnan & Mitragotri, 2020). Absorption by intercellular and transcellular ways happens directly through the SC, while in the trans-appendageal route particles enter using the various appendages, which include sweat glands, hair follicles, and sebaceous glands present in the skin. These appendages are only a small part of the total skin surface, but their contribution to nanoparticle absorption can be significant (Krishnan & Mitragotri, 2020).

Two characteristics that influence the nanoparticles' interaction with the skin are their size and charge. Relatively to the charge, there is a widespread belief that positively charged particles will interact with the negatively charged *stratum corneum* and pass through it easier. Still, there is evidence that either negatively or positively charged particles can be absorbed (Krishnan & Mitragotri, 2020). Regarding the particles' size, it has been shown to influence drug delivery into the skin significantly. Bigger particles, with a diameter of 600 nm or above, cannot enter the deeper layers of the skin. However, they can deposit in the SC and form a lipid film when dried (Danaei, et al., 2018). A diameter of 300 nm or below allows the particles to deliver their content to some extent into deeper layers, but the maximum delivery has been seen in particles with 70 nm or below (Danaei, et al., 2018). Particles with sizes ranging from 10-210 nm often deposit in the follicles and enter through the trans-appendageal route (Krishnan & Mitragotri, 2020) (Danaei, et al., 2018).

Among the existent types of nanoparticles, lipid-based ones have proven to be a good choice in treating skin diseases and skin cancer (Danaei, et al., 2018). Their constitution allows their blending with the SC initiating drug release. Some authors have reported that this type of particle cannot pass until the deeper layer of the epidermis, not reaching the blood circulation and accumulating in the skin instead. For treating skin diseases, this can be used as an advantage since it retains the drug and extends the time of its action in the same location of the lesion (Danaei, et al., 2018). Thus nanoparticles, as liposomes, are promising systems for drug delivery in skin cancer therapies (Danaei, et al., 2018) (Dianzani, et al., 2014).

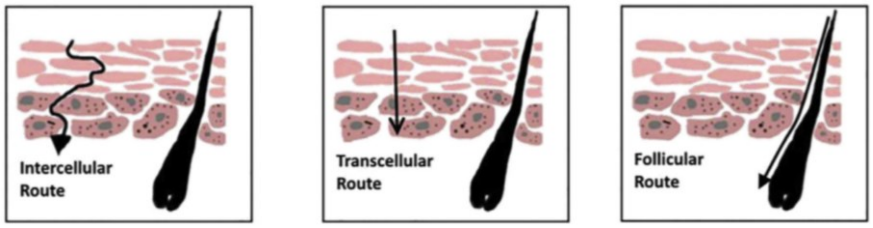

Figure 1.3 - Possible routes of skin crossing *(Krishnan & Mitragotri, 2020)*

1.8 Lipid-based nanoparticles

Lipid-based nanoparticles have been a topic of great interest in nanomedicine, especially in drug delivery and cancer therapies. The first anticancer drug nano system commercially used is a liposome formulation for doxorubicin encapsulation (Doxil®) (Barenholz, 2012). Their constituents are usually phospholipids, phosphocholine, and cholesterol, by themselves or in combination. Inside their core, they can encapsulate hydrophobic or hydrophilic molecules and present very low toxicity. They have also been successful in prolonging the half-life and controlled release of drugs. Chemical changes to their formulations can even make them avoid immune detection, improve the solubility of the drug, make them sensitive to pH, or even make them recognize tumor cells by adding antibodies (García-Pinel, et al., 2019).

Between the lipid-based nanoparticles, it is possible to identify three groups: liposomes, solid lipid nanoparticles, and nanostructured lipid carriers (García-Pinel, et al., 2019).

Liposomes are circular soft vesicles organized in one or more bilayer membranes due to their amphipathic properties, with a size range between 50 and 450 nm (Patra, et al.,

2018). They are constituted by phospholipids and can have other additional components, such as cholesterol, which can decrease the flexibility of the nanoparticle and increase the permeability of hydrophobic drugs through the bilayer (García-Pinel, et al., 2019). The polar group of its phospholipids can be positive or negative, and its hydrophobic chain can have different lengths. The assembly of these particles happens spontaneously when their dry form is placed into an aqueous solution (Jeong, et al., 2021). Due to their biocompatibility and biodegradability, liposomes are the most studied delivery system (García-Pinel, et al., 2019) and already account for many applications in the pharmaceutical and cosmetic industries (Patra, et al., 2018).

Solid Lipid Nanoparticles are a more recent drug delivery system. Its main difference from liposomes is that the lipids that they are made of, such as mono, di, and triglycerides, fatty acids, and glyceride mixtures, are in the solid state at room and body temperatures (García-Pinel, et al., 2019). These solid lipids form a matrix stabilized by surfactants and polymers. These particles have a size ranging from 50 to 1000 nm. These particles can be used for drug delivery and have advantages such as site-specific targeting, are stable for long periods, can control the release of both lipophilic and hydrophilic drugs, offer good protection for more unstable drugs, are low cost, and have low toxicity (García-Pinel, et al., 2019). In turn, they have as disadvantages its moderate drug loading capacity and present some drawbacks in the drug expulsion during storage (García-Pinel, et al., 2019).

Regarding Nanostructured Lipid Carriers, they correspond to the second generation of lipid-based nanoparticles that was developed in the attempt to improve Solid Lipid Nanoparticles. They are composed of a blend of solid and liquid lipids, such as glyceryl tricaprylate, ethyl oleate, isopropyl myristate, and glyceryl dioleate (García-Pinel, et al., 2019). In this way, compared with the Solid Lipid Nanoparticles, they present higher loading capacity and improve their limitations in drug storage. Their size ranges from 10 to 1000 nm.

1.9 Skin models

Clinical trials are dispendious and result in numerous failures (Esmaeili, et al., 2021). Therefore, to achieve an optimal transdermal drug delivery formulation is essential to test it in its development stages in well-defined skin models. The possible options for these tests are animal, *ex vivo,* and *in vitro* testing. Changes in the regulation of animal testing due to its ethical issues have led cosmetic and pharmaceutical industries to search for

other solutions, using *in vitro* skin models for studies of permeation, penetration, skin irritancy, and toxicity more and more requested (Flaten, et al., 2015) (Yun, et al., 2018).

In vitro skin models are composed of cells, by themselves or accompanied by biomaterials, grown under controlled conditions. Among these models, it is possible to identify two groups: two-dimensional (2D) and three-dimensional (3D) cultures.

In 2D cultures, cells grow as a flat monolayer. This technique is helpful for testing phototoxicity, corrosivity, irritancy, and permeability. It is also a valuable tool for further understanding molecular signaling, cellular morphology, and drug innovation (Yun, et al., 2018). As a 2D skin model, a culture of only keratinocytes, mimicking the human epidermis, has exhibited high reproducibility in assessing risks (Mathesa, et al., 2013). Despite these advantages, not all the results from 2D *in vitro* models are translatable to *in vivo* systems (Randall, et al., 2018). Furthermore, they lack some factors such as mechanical forces, spatial orientation, and oxygen, nutrient and signaling gradients, characteristics of an *in vivo* environment (Randall, et al., 2018).

In turn, 3D *in vitro* skin models or full-thickness models are more sophisticated and can be used to test drug efficacy, although, due to their complexity, they are also harder to standardize (Mathesa, et al., 2013). In these models, it is possible to represent an epidermis and a dermis, enabling cellular cross-talk between different cell types and interfaces between cell-to-cell, cell-to-matrix, and cell-to-environment, critical factors for cellular function (Randall, et al., 2018) (Mathesa, et al., 2013). As a result, cells have been shown to be more physiologically responsive when in a 3D culture than in 2D culture (Randall, et al., 2018).

3D skin models can be engineered with or without a scaffold. Scaffold-free models result in spheroids formed from cells that are prevented from adhering to a substrate, so they self-assemble into cell aggregates (Randall, et al., 2018) (Quarta, et al., 2021). They recreate many organ or tumor tissue features, such as the deposition of the extracellular matrix (ECM), cell-to-cell interactions, and the formation of nutrient, waste, and gas gradients (Randall, et al., 2018). On the other hand, 3D models with scaffolds offer valuable advantages such as providing an environment with characteristics more similar to the *in vivo* ECM, reproducing the cell-to-matrix interactions related to phenomena such as cytoskeletal organization, gene expression, nutrient diffusion, pH, and hypoxia (Quarta, et al., 2021). The scaffolds can be made of one or a combination of natural and synthetic polymers. They can be fabricated through various techniques, such as freeze-drying, 3D bio-printing, electrospinning, and microfluidic systems (Yun, et al., 2018).

Among the materials that can be used to produce these structures, natural polymers, such as collagen, silk, alginate, chitosan, fibrin, and elastin, have shown to have advantageous characteristics, their biocompatibility being the most remarkable one (Randall, et al., 2018).

Moreover, besides 3D skin models of healthy cells, there is also the possibility of creating models for diseases such as skin cancers, inflammatory illnesses, and damaged skin (Abd, et al., 2016). These models allow the analysis of the delivery and effects of topical treatments and also study important molecular mechanisms of a particular disease. Among diseased skin models, the most popular models are tumor spheroids and scaffold-based models (Esmaeili, et al., 2021) (Quarta, et al., 2021) (Abd, et al., 2016).

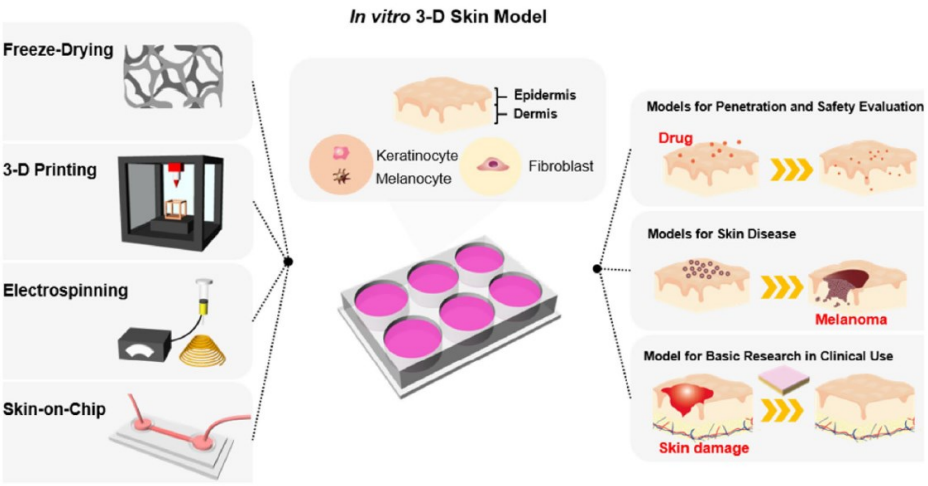

Figure 1.4 - In vitro 3D skin models methods of assembly and their applications (Yun, et al., 2018)

1.10 Collagen hydrogels as scaffolds for 3D skin models

Hydrogels are cross-linked non-soluble polymer structures that can absorb and retain substantial amounts of water. Due to their properties and versatile fabrication methods, they have been widely used in biomedicine and engineering (Wang, et al., 2020). They have shown to be great allies as tools for developing therapies through multiple approaches, such as drug delivery systems, smart hydrogels, hydrogel-based implants, organ-on-a-chip, and 3D models (Esmaeili, et al., 2021).

As scaffolds for 3D models, hydrogels can resemble the ECM and be a suitable place to accommodate cells. They can be composed of various materials. Among them, collagen is one of the most studied and used (Randall, et al., 2018) (Esmaeili, et al., 2021) (Lee, et al., 2017).

Collagen is the primary component of the dermis ECM. Its outstanding characteristics, such as biocompatibility, biodegradability, and versatility, make it one of the most used biomaterials in biomedical applications (Lee, et al., 2017) (Lin, et al., 2019). Additionally, it is easy to extract and is available in large quantities from the tendon, skin, intestine, cornea, and blood vessels of some mammalian animals as well as marine organisms (Lin, et al., 2019).

Collagen hydrogels form an aqueous-based colloidal gel where collagen is the main solute and water is the solvent. Cells and bioactive components can be directly integrated into its matrix during the fabrication process (Lin, et al., 2019). Generally, in skin models, fibroblasts are incorporated into the hydrogel to resemble the dermis (Mathesa, et al., 2013) (Lee, et al., 2017).

The main issue in collagen hydrogels is their weak mechanical properties, which influence cell behavior (Sarrigiannidis, et al., 2021). It has low stiffness, being susceptible to physical contraction resulting from the fibroblast exert forces, and it is prone to enzymatic degradation, making them unstable for long-term cultures (Randall, et al., 2018) (Sarrigiannidis, et al., 2021). These limitations can be ameliorated by collagen crosslinking or by combining it with other polymers (Sarrigiannidis, et al., 2021).

Nevertheless, collagen hydrogels are still the most used model to mimic healthy and diseased skin (Randall, et al., 2018). There are already commercial full-thickness skin models based on collagen, such as Phenion® (Henkel, Germany) and NeoDerm® (Tegoscience, Korea) (Yun, et al., 2018).

2. Scope of the thesis

In this work, two main activities have been carried out exploiting nanotechnologies and bioengineering approaches: the first is the development, characterization, and optimization of phosphatidylcholine-based vesicles for the encapsulation of 5-aminolevulinic acid.

The second activity is the creation of a 3D skin cancer model composed of an agarose-collagen blend hydrogel embedded with melanoma spheroids.

Finally, the drug nanocarrier developed has been tested in the 3D model.

3. Materials and Methods

3.1 Chemicals and reagents

For the synthesis of the nanovesicles, the reagents and chemicals used were 1,2-dimyristoyl-sn-glycero-3-phosphocholine (DMPC), 1,2-dilauroyl-sn-glycero-3-phosphocholine, 12 carbons alkyl chain (DLPC 12), 1,2-dilauroyl-sn-glycero-3-phosphocholine, 14 carbons alkyl chain (DLPC 14), 1,2-Distearoyl-sn-glycero-3-phosphorylethanolamine (DSPE), and 1,2-dioleoyl-sn-glycero-3-phosphocholine (CisPC), all purchased from Avanti Polar Lipids, and L-α-lyso-Lecithin, from Egg Yolk (Lecithin) from Merk EDM Millipore. Ethanol was acquired at VWR Chemicals. The Ultra-pure water was obtained from the Ultrapure water purification system at the lab this work was developed. Agarose, Limonene, Fluorescamine, and 5-aminolevulinic acid were purchased from Sigma-Aldrich. The cell lines of human melanoma cell line (HBL), human keratinocytes cell line (HaCaT), and Michigan Cancer Foundation-7 (MCF7) breast carcinoma were obtained from American Type Culture Collection (ATCC). Type I collagen was kindly provided by the group of Prof. Alessandro Sannino from the University of Salento, Lecce, Italy.

3.2 Synthesis and loading of phosphatidylcholine-based vesicles

Initially, several types of phospholipids (DMPC, DLPC 12, DLPC 14, DSPE, CisPC, Lecithin) and cholesterol were tested, and two different preparation approaches were considered, the ultrasonication and the solvent injection method. After these preliminary tests, the solvent injection method was selected as it allowed to obtain stable, monodisperse, and biocompatible vesicles. A mixture of the following lipids, DMPC, DLPC 14C, and lecithin (mixed according to the weight ratios 1:1:1), was selected as the lipid composition of the vesicles.

3.2.1 Invasomes

The vesicles made of DMPC, DLPC 14C, and lecithin were named Invasomes and prepared as follows.

The three components (10 mg of each lipid) were dispersed in 3 mL of ethanol. To this mixture, 15 μL of limonene was added, which will posteriorly provide more flexibility to the lipid bilayer wall. The final mixture was split into 3 vials.

Using a syringe pump, 5 mL of ultrapure water were added, drop by drop, to each vial while vigorously stirring the sample using an orbital shaker. Finally, the samples were left stirring overnight at room temperature (RT).

3.2.2 Single phospholipid vesicles

Single lipid vesicles, made of either DMPC, DLPC 12C, DLPC 14C, DSPE, CisPC, or lecithin, were also prepared to assess the cytotoxicity of the individual lipid component.

For each kind of particle, 10 mg of each lipid were dissolved into 1 mL of ethanol. The samples were placed in the orbital shaker, where 5 mL of water was added, as reported in the previous section. The samples were left shaking overnight at RT.

3.2.3 Encapsulation of Rhodamine

To make the vesicles optically detectable, a fluorescent dye, Rhodamine 110, was encapsulated inside the Invasomes.

In detail, the mixture of phospholipids was dissolved in 3 mL of ethanol containing 15 µL of limonene, and, as already reported, it was split into 3 vials. Into each vial, 30 µL of Rhodamine 110 (2 mM in ethanol) were added. The samples were then placed in the orbital shaker, followed by the dropwise addition of 5 mL of ultrapure water.

3.2.4 Encapsulation of 5-ALA

To encapsulate the prodrug 5-ALA into the nanoparticles, the protocol was slightly modified in order to increase the encapsulation efficiency.

5-ALA, as a zwitterion, possesses two ionization sites (pK_a 4.0 and pK_b 8.20). According to the literature, unionized 5-ALA can diffuse through the lipid bilayers freely, while protonated 5-ALA cannot diffuse through the lipid bilayer freely (Zhang, et al., 2016). Therefore, a mechanism of active loading through a pH gradient can be used to entrap more molecules of 5-ALA inside the vesicles. For this aim, the nanovesicles were prepared using an acidic solution (phosphate buffer solution pH 4.5) instead of ultrapure water. At pH 4, the drug is in its protonated form. When the pH of the medium is brought to neutral by adding NaOH 1M, 5-ALA turns from the protonated status to the unionized

status making them able to cross the bilayer of the nanoparticles. When a molecule of 5-ALA enters a vesicle, it turns into its pronated form again due to the acidic environment. Consequently, the molecule loses its ability to cross the bilayer and stays entrapped inside the nanoparticle (Zhang, et al., 2016).

In detail, the mixture of phospholipids dissolved in ethanol was prepared and split into 3 vials. In each vial, 5-ALA (5 mg/mL dissolved in ultrapure water) was added. The samples were then placed in the orbital shaker, followed by the dropwise addition of 5 mL of phosphate buffer solution (pH 4.5). The sample is left under stirring at 700 rpm for 30 minutes, then the pH gradient is applied: NaOH (1M) is added until the pH of the sample reaches a value close to 7.4. Finally, the sample is left stirring overnight and then dialyzed as described in 2.3.2.

3.3 Characterization of the Nanovesicles

3.3.1 Dialysis of the samples

After the preparation, the samples were always dialyzed to remove any residues and non-encapsulated drugs or dyes.

In this aim, the sample is transferred into a dialysis bag (Sigma-Aldrich Dialysis Tubing Cellulose Membrane of 25 mm width and 14000 kDa molecular cutoff), which is then immersed into the dialysis box. The box was placed under magnetic stirring overnight in a cold room.

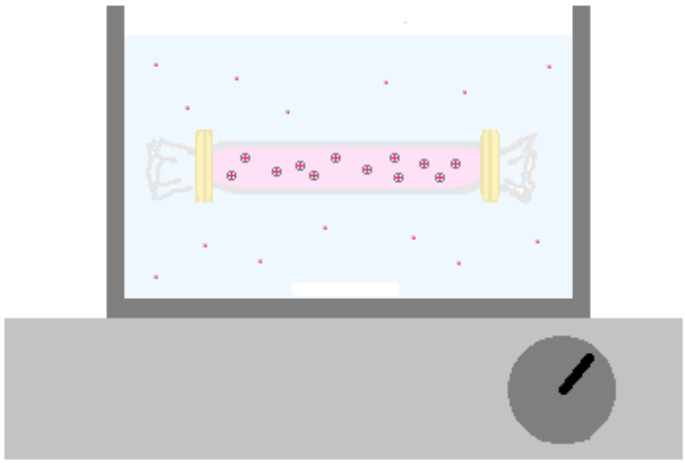

Figure 3.1 - Representation of the dialysis setup

3.3.2 Encapsulation efficiency of Rhodamine

To calculate the encapsulation efficiency (EE) of Rhodamine, an indirect measurement method was used.

The water resultant from the dialysis was recovered, and its fluorescence was measured by a fluorimeter (Cary Eclipse). Plotting the fluorescence value on a Rhodamine calibration curve previously done, the concentration of Rhodamine that was not encapsulated is determined.

Then, known the feeding concentration of rhodamine (equivalent to the maximum concentration of rhodamine that can be internalized), the encapsulated amount was estimated and reported as EE according to the formula presented in Equation 3.3.2 – 1.

$$EE(\%) = \frac{(\,Maximum\ concentration\ -\ Dialysis\ water\ concentration)}{Maximum\ concentration} \times 100 \qquad (3.3.2 - 1)$$

3.3.3 Quantitative assay of 5-ALA and Encapsulation efficiency

To detect 5-ALA rapidly and accurately, a modified Flurescamine assay was established. The method is based on the conversion of 5-ALA into a fluorescent derivative after reacting with Fluorescamine, as represented in Figure 3.2. As in the case of Rhodamine, the non-encapsulated drug was first quantified, and then, by subtracting the feeding amount, the encapsulated concentration was obtained.

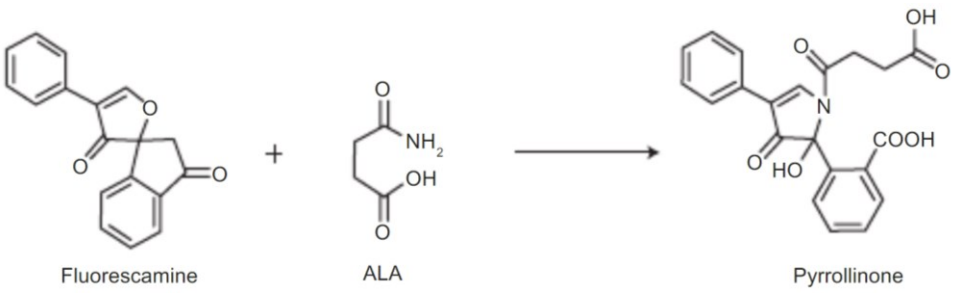

Figure 3.2 - Reaction between Fluorescamine and 5-ALA

The protocol consists of mixing 300 µL of the sample, 270 µL of Fluorescamine (0,1% in acetonitrile), and 45 µL of borate buffer solution (pH 8.0). The mixture was vortexed for 5 seconds and put into a dark environment for 5 minutes for the reaction to occur.

The Fluorescamine assay was performed with the dialysis water, with the feeding solution of 5-ALA, and with all the standard solutions prepared for the calibration curve.

Indeed, as already described in the case of Rhodamine, a calibration curve with 5-ALA (concentrations ranging from 0,5, 1, 5 to 25 μg/mL) was prepared.

After the incubation time, 200 μL of each mixture were transferred to a multi-well plate. The fluorescence of the mixture was then measured (excitation wavelength at 380 nm and emission wavelength at 480 nm) using a multi-well reader CLARIO starPlus BMG LABTECH.

Finally, to achieve the value of the EE the formula presented in Equation 3.3.3 – 1 is applied.

$$EE(\%) = \frac{(\,Maximum\ concentration\ - Dialysis\ water\ concentration)}{Maximum\ concentration} \times 100 \qquad (3.3.3 - 1)$$

3.3.4 Loading Capacity

The loading capacity corresponds to the mass of the drug that nanovesicles are able to entrap per unit of mass of the nanovesicles.

Primarily, samples of Invasomes loaded with the drug were lyophilized, and their dry mass was determined. The mass of the sample entrapped was calculated by multiplying the feeding drug mass by the EE of the sample. Posteriorly, to determine the LC, the formula presented in Equation 3.3.4 – 1 was applied.

$$LC = \frac{mass\ of\ entrapped\ drug}{mass\ of\ the\ sample} \qquad (3.3.4 - 1)$$

3.3.5 Dynamic light scattering

The size of the nanovesicles was measured using the dynamic light scattering (DLS) method.

DLS is an optical technique used for analyzing dynamic properties and size distribution of a broad range of physical, chemical, and biological materials suspended in a liquid. It is a non-destructive and relatively fast measurement and requires a small amount of sample. When in suspension, the particles move randomly as a result of Brownian motion. There is a correlation between particle size and particle speed, where smaller particles diffuse faster, and bigger particles diffuse slower, so monitoring their movement over time can provide information about the size (Minton, 2016) (Stetefeld, et al., 2016). Other factors influence its movement, such as temperature and solvent viscosity, therefore, accurate knowledge of these properties is mandatory for this measurement (Minton, 2016).

The instrument setup is represented in Figure 3.3. The analysis starts with a monochromatic laser that illuminates the sample, which scatters the light beam, generating a scattered light intensity signal. Since suspended particles undergo Brownian motion, as referred before, this results in fluctuations of the signal over time, where faster variations correspond to the presence of smaller particles while slower variations indicate the presence of larger particles.

The signal reaches a photon detector linked to the correlator that then correlates intensity fluctuations with time on a nanosecond and microsecond scale to determine how rapidly these variations occur. The change of intensity along the time allows a computing correlation from where it is possible to get the translational diffusion coefficient (D_t). Knowing this value, it is possible to calculate the radius of the particles using the Stokes-Einstein equation (Equation 3.3.5 – 1).

$$Dt = \frac{k\,T}{6\pi\,\eta\,R} \qquad (3.3.5 - 1)$$

Where D_t is the translational diffusion coefficient, k is the Boltzmann's constant, T is the absolute temperature, η is the viscosity of the solvent, and R is the particle's radius (Minton, 2016) (Instruments, 2022).

The data resultant gives information about the average hydrodynamic size of the particles and size distribution that can be weighted by intensity, volume, or number. The data is generally reported by intensity, which is proportional to the particle's radius in the power of 6 (R^6), making it very sensitive to large particles or aggregates. Another information the DLS provides is the polydispersity index (PDI), which estimates the width of the distribution of the sizes of the particles (Minton, 2016).

It is important to point out that the model used by this equipment is only accurate for spherical particles, working only in approximations for macromolecules that deviate significantly from this shape (Minton, 2016).

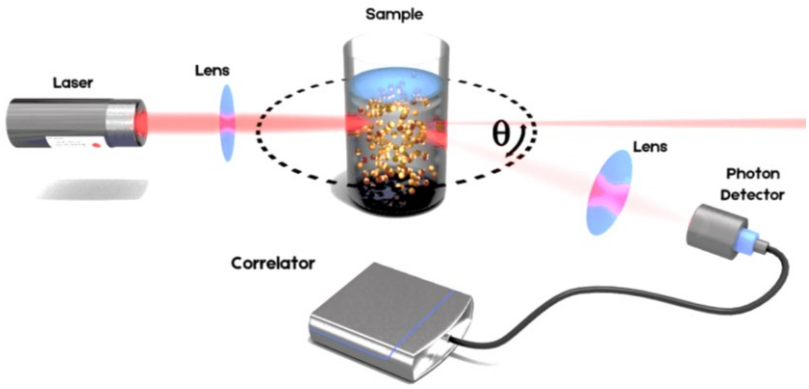

Figure 3.3 – Schematic representation of a DLS setup *(Instruments, 2022)*

In some DLS equipment is also possible to measure the Zeta potential (ZP) of the sample. This property is related to the charge of the surface of the nanoparticle, its knowledge is useful to predict and optimize the long-term stability of a suspension or emulsion as well as understand its performance (Kaszuba, et al., 2010).

The particles dispersed in an aqueous media generally carry an electric charge. This induces the adsorption of free ions of the opposite charge on the surface of the particle, forming an electric double-layer. This surrounding layer can be divided into two layers – the internal layer composed of ions strongly attracted to the particle called the stern layer, and an outer layer, the diffuse layer, where the attraction of the ions is weaker. In Figure 3.4, it's possible to observe a schematic representation of the electrical double layer.

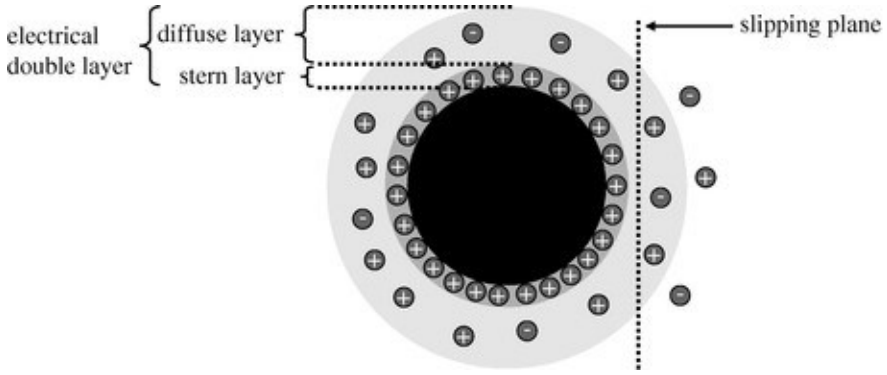

Figure 3.4 - Schematic representation of the electric double-layer *(Kaszuba, et al., 2010)*

In the diffuse layer, there is a frontier that divides ions strongly attached from ions not bound to the particle's surface. This limit is called the slipping plane and is where ZP is measured. This border also limits the ions that accompany the particle as it moves through the medium because of the Brownian motion or sedimentation (Kaszuba, et al., 2010) (Sciences, 2022).

In a ZP measurement, a disposable folded capillary cell with two electrodes in contact with the sample is used. Particles are attracted to the electrode with the opposite charge and will move towards it with a velocity proportional to their ZP. The sample is irradiated with a laser which indirectly determines the speed through the Doppler frequency shift on the scattered light (Sciences, 2022). Knowing its velocity, it is possible to calculate the value of electrophoretic mobility (U_E), and by applying Henry's equation (Equation 3.3.5–2), it is converted into the ZP.

$$U_E = \frac{2\varepsilon\zeta\, F(ka)}{3\eta} \qquad (3.3.5-2)$$

Where U_E is the electrophoretic mobility, ε is the dielectric constant of the dispersant, η is the viscosity of the dispersant, $F(ka)$ is the Henry's function, and ζ is the ZP (Kaszuba, et al., 2010).

In this thesis work, the DLS and ZP measurements were performed using a Zetasizer Nano ZS90 Malvern Instruments Ltd. The dispersant was water at a temperature of 25°C using. Each sample was measured in triplicate, and the average value was used. The

measurements were performed on day 1 (after the dialysis) and at different time points to monitor the stability of the vesicles.

3.3.6 Transmission Electron Microscopy

The transmission electron microscopy (TEM) technique is a powerful tool for providing detailed information concerning the structural characteristics of nanoscale structures, such as nanoemulsions, nanoliposomal delivery systems, nanoparticles, and nanofibers. It provides qualitative information about the sample's shape and can also be used as a quantitative method to determine the particle size and distribution.

Transmission electron microscopes employ a particle beam of electrons to visualize samples, generating a highly magnified image. This equipment can magnify objects up to 2 million times, which is valuable in the biological and medical fields.

An electron gun at the top of a TEM projects electrons that travel through the microscope's vacuum tube. Electromagnetic lenses are used to concentrate the electrons into a very thin beam. The electrons reach the sample and react with it, losing energy depending on the sample's properties, such as density, composition, and crystallinity (Scientific, s.d.). The transmitted electrons reach the fluorescent screen, which is coated with a chemical that turns bright when electrons come into contact with it. The intensity of the bright spot depends on how much energy the electron has, providing contrast to the resulting image. This image can then be studied directly within the TEM or photographed. Figure 3.5 shows a diagram with the basic components of a TEM.

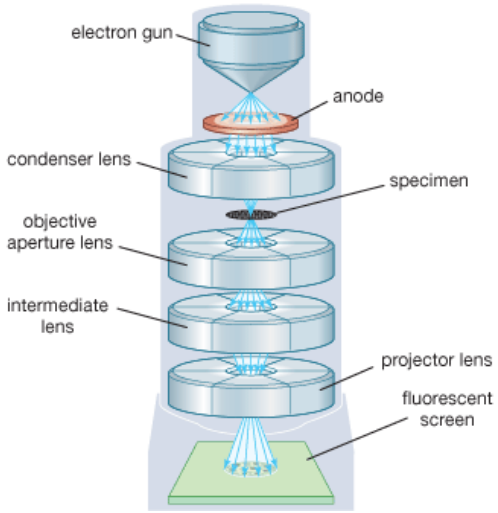

Figure 3.5 - Typical structure of a Transmission Electron Microscope

TEM analysis of the vesicles was performed with a JEOL Jem1011 microscope (Tokyo, Japan) operating at an accelerating voltage of 100 kV. The samples were dropped onto carbon-coated copper grids that were let dry under air O.N. before being imaged.

3.3.7 Thermogravimetric analysis

A thermogravimetric analysis (TGA) was conducted to determine the sample's thermal stability.

The TGA is a characterization technique in which the mass variations of a sample are measured as a function of temperature or time, providing quantitative and qualitative information about its physical changes. The heating of the sample is usually done at a constant rate, but the analysis can also be done with a constant temperature or with a non-linear temperature program, depending on the information requested. The atmosphere used in the test plays an important role and can be inert or oxygen-rich (Bottom, 2008).

The equipment comprises a sample pan placed inside a sealed furnace and connected to a scale. The scale can be a hanging scale, a top-loading scale, a horizontal scale, or a compensating scale. A temperature controller regulates the heating system according to the program settled, and a thermometer inside the furnace sends information to the temperature controller and to the recorder.

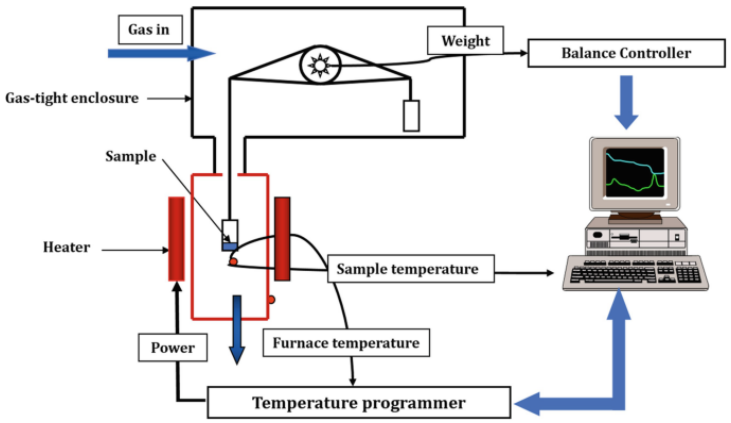

Figure 3.6 - Representation of a TGA equipment setup *(Akash & Rehman, 2020)*

The results of a TGA measurement can be presented as a TGA curve showing the percentage of weight loss plotted against temperature or time, or it can also be shown as the rate of weight loss plotted against the variation of temperature, being this one the

differential thermogravimetric (DTG) curve. The DTG curve is the first derivative of the first option and allows easier identification of when the mass changes occur. These two ways of presenting the results complement each other (Bottom, 2008).

Thermogravimetric analysis (TGA) of the nanovesicles was performed using SDT Q600 equipment (TA Instrument, New Castle, DE, USA), with a heat ramp of 5 °C/min and an airflow rate of 100 mL/min.

3.3.8 Diffusion of the Invasomes into ex-vivo skin

The initial tests of the particles' diffusion into the skin were done in samples of *ex-vivo* pig skin. The scheme presented in Figure 3.7 represents the apparatus developed to perform these tests, inspired by a Franz diffusion cell.

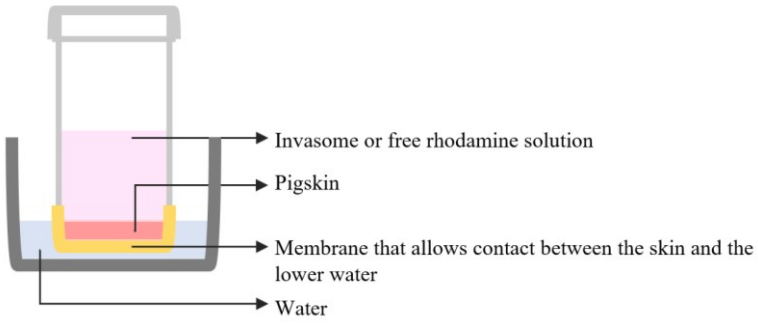

Figure 3.7 - Representation of the setup used to study the diffusion of Invasomes into skin

The apparatus consists of a plastic tube equipped with a membrane at the bottom over which the pig skin is glued around the edges. Disks of pig skin with the same diameter as the internal wall of the tube were previously cut. The tube is then placed inside a small beaker filled with ultrapure water. In the upper part of the tube, the fluorescent samples are loaded, and the fluorescence decay was measured over time (time 0, 30 minutes, 1 hour, 2 hours, 3 hours, and 4 hours). Two types of samples were analyzed, Invasomes loaded with Rhodamine and free Rhodamine.

The percentage of fluorescence decrease was calculated according to the Equation 3.3.8–1:

$$Fluorescence\ decrease\ (\%) = \frac{i\,FI - r\,FI}{i\,FI} \times 100 \qquad (3.3.8-1)$$

Where iFI is the initial fluorescence intensity and rFI is the residual fluorescence intensity.

Additionally, after the fluorescence analysis, the skin disks were recovered and observed under the fluorescence microscope.

3.4 Cellular tests

Cellular studies were performed with human keratinocytes and melanoma cells, namely HaCat and HBL cells, respectively, to characterize the interactions among the nanovesicles herein developed and the cells, with particular emphasis on the effects of the NPs on cell viability and their potential in photodynamic therapy. Preliminary studies to assess the biocompatibility of the single lipid-made vesicles were also performed with human breast cancer cells (MCF7 cells), HaCat, and HBL cells.

Additionally, cellular studies were performed with 3D spheroids of human melanoma cells embedded into agarose hydrogel to investigate the capability of the Invasomes to penetrate through the gel matrix and into the 3D structure.

At the beginning of the thesis work, the human basal cell carcinoma, TE 354.T was considered. Indeed, the basal cell carcinoma is one of the most common skin tumors and is commonly treated with 5-ALA and photodynamic therapy in the clinics (Łasińska, et al., 2022). Unfortunately, the cells' extremely slow replication time was incompatible with the studies intended to carry out; therefore, this cell line was not used.

3.4.1 Cell culture conditions

The three human cell lines were grown in DMEM medium supplemented with 10% fetal bovine serum (FBS), 2 mM glutamine, 100 IU/mL of penicillin, and 100 μg/mL of streptomycin. The MCF7 were cultured in an incubator at 37° C in a humidified atmosphere with 5% CO_2.

When approximately 80% of cell confluence was reached, the medium was removed, and the flask was washed with PBS to remove residues of the culture medium containing trypsin inhibitors. At this point, trypsin 0.25% - EDTA 0.02% was added to detach cells from the flask's wall and to separate them from each other upon incubation at 37ºC for 5 minutes. Trypsin is a proteolytic enzyme that acts by breaking the peptide

bonds that the extracellular proteins establish with the substrate on which the cells are anchored. Then the cells were resuspended in a complete medium to stop the action of the trypsin. An aliquot of this cellular suspension was plated into a flask to let the cells adhere, grow, and expand.

3.4.2 Cell freezing and thawing

To freeze the cells, a freezing medium consisting of FBS (40%), RPMI 1640 (or DMEM) (50%), and DMSO (10%) was prepared. Once confluency was reached, cells were trypsinized and centrifuged at 500 *g* for 6 minutes at 4 ºC; the supernatant was removed, and the cells were resuspended in 1 ml of freezing medium and transferred to freezing vials. After that, the freezing vials containing the cells were placed in the freezer at -20 ºC O.N. and finally transferred to -80 ºC. To defrost the cells, the vials were removed from the freezer and placed in a thermostatic bath at 37ºC for a few minutes to allow rapid and complete thawing. Soon after, the cells were centrifuged at 500 g for 6 minutes at room temperature. The supernatant was removed, and the pellet was re-suspended in 6 ml of medium described in the previous paragraph and plated into a cell culture flask.

3.4.3 MTT assay

The cytocompatibility of the nanovesicles was determined by the assay of 3- [4,5-dimethylthiazol-2-yl] -2,5-diphenyl tetrazolium bromide, usually called tetrazolium salt thiazolyl blue (MTT). It is based on the reduction of tetrazolium, a yellow water-soluble substance, into formazan, an insoluble purple substance. A mitochondrial enzyme, named succinate dehydrogenase (SDH), together with the nicotinamide adenine dinucleotide (NAD), is responsible for the reduction of MTT. This process occurs in metabolically active cells. Thus, the amount of formazan is directly proportional to the number of living cells (Plumb, 2004) (Tolosa, et al., 2014).

In detail, 2.5 x 10^4 cells suspended in 200 µl culture medium were seeded into each well of 96 multiwell plates for 24 hours. Then, the nanoparticles were added at different concentrations (from 50 to 500 µg/mL, each point in triplicate) and incubated at 37 ºC. After 24 h, the culture medium was removed, the cells were washed with PBS

twice, and 200 µl of fresh serum-free medium containing 2 mg/mL MTT was added to each well. After 3 hours of incubation at 37°C, the culture medium was removed from the wells, and 200 µl of DMSO was added to dissolve the formazan salts. The plate was stirred for a few minutes at ambient temperature, and the solution's absorbance was measured by the spectrophotometer at a wavelength of 570 nm. To determine the percentage of cell viability, the treated samples were compared to the control samples according to the Equation 3.4.3 – 1:

$$Viability\ (\%) = \frac{Absorption\ of\ the\ treated\ sample}{Absorption\ of\ the\ control\ sample} \times 100$$

(*3.4.3* – 1)

3.4.4 Administration of the ALA-loaded nanovesicles and Photodynamic therapy

To assay the biological efficacy of the nanovesicles, 2.5 x 10^4 cells (both HBL and HaCat cells) suspended in 200 µl culture medium were seeded into each well of 96 multiwell plates for 24 h. Then, the 5-ALA-loaded nanovesicles and free 5-ALA were added to the cell medium to reach a final concentration of 25 µg/mL. The amount of prodrug administered was fixed to 25 µg/mL, in accordance with previously published works (Li, et al., 2019). Empty vesicles were also added as a control sample. The cells were incubated for 3 h. Then the medium was removed and replaced with 100 µL of Leibovitz medium, and the cells were irradiated for 15 minutes with a red lamp emitting at 630 nm (power supply 11 Volt) (Figure 3.8). Soon after, the cells were processed accordingly:

- fresh medium was added, and the cells were transferred into the incubator for an additional 24 h prior to performing the MTT assay (as described in 2.4.3);
- to measure the reactive oxygen species, the cells were prepared as reported in the following section (2.4.6).

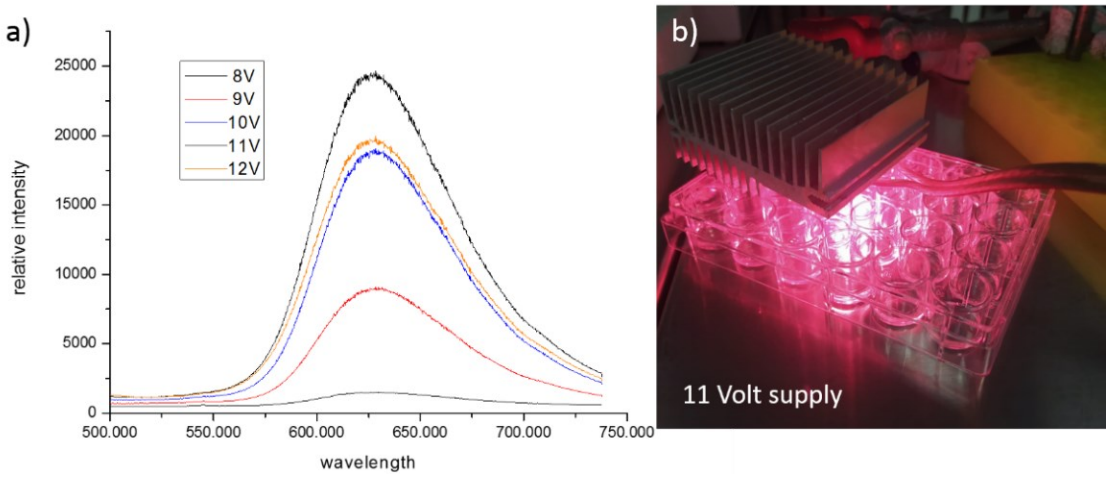

Figure 3.8 - a) Emission Spectrum of the lamp at different Volt supply; b) Image of the lamp applied to the cells.

3.4.5 Measurement of Reactive Oxygen Species (ROS)

To detect the changes in intracellular ROS levels, 2',7'- dichlorofluorescein diacetate (DCFH-DA, Sigma-Aldrich) staining was used (Kim H, 2020). DCFH-DA is a stable, fluorogenic, and non-polar compound that can readily diffuse into the cells and get deacetylated by intracellular esterases to a non-fluorescent 2',7'-dichlorodihydrofluorescein (DCFH) which intracellular ROS later oxidizes into highly fluorescent 2',7'-dichlorofluorescein (DCF). The intensity of fluorescence is proportional to intracellular ROS levels.

After the treatment with encapsulated and free 5-ALA and the light irradiation, the cells were washed once with fresh DMEM and twice with 1x PBS. Then, they were incubated with DCFH-DA (10 µM) for 30 min and rinsed with PBS. Representative fluorescent images for each well using the green fluorescent protein (GFP) channel were taken on an Evos M7000 fluorescence microscope. After taking images, PBS was removed, and a radioimmunoprecipitation assay (RIPA) buffer was added to each well. The collected cells were incubated at -80 °C for 20 minutes and then centrifuged at 21,130 g for 10 minutes at 4 °C. The collected supernatant was transferred to a black 96-well plate, and the fluorescence intensity was measured using the CLARIO star Plus microplate reader at an excitation wavelength of 485 nm and an emission wavelength of 530 nm. After fluorescence recording, 5 µL of supernatant were transferred to a transparent 96-well plate containing 195 µL of the protein assay solution to measure the protein concentration using the BCA assay. The fluorescence intensity was normalized to the protein concentration.

3.4.6 Preparation of agarose-collagen hydrogels

Agarose was dissolved in sterile phosphate-buffered saline (PBS, pH 7.4) and heated on a hot plate to obtain a 1% (w/v) stock solution.

Type I collagen was extracted and purified from Nile Tilapia dermis (Gallo, et al., 2022). An aqueous suspension (1% w/v) containing the crosslinking agent was prepared by magnetic stirring. Then it was stored at 4 °C. The blended hydrogel was prepared inside the wells of a 24-well plate, where each well was loaded to a final volume of 0.4 mL.

The warm agarose solution (at around 45 °C, the gel point is at 36 °C) was added to the collagen suspension to obtain 0.18% agarose and 0.1% collagen. The mixture in each well was gently stirred with a glass rod and allowed to gel at room temperature. All the glassware was sterilized in an autoclave before use, and the hydrogels were prepared under a laminar flow hood to preserve sterility.

3.4.7 Encapsulation and growth of melanoma tumor spheroids in the agarose-collagen hydrogel

The melanoma cells were detached with tripsine, counted, and added to the warm (~45°C) blend solution of agarose/collagen hydrogels at a density of 5 x 10^4 cells/mL in complete growth medium. The cell suspension containing agarose and collagen was let to gel into the well plate. After gelation, 1 mL of DMEM was added over the cell-embedded hydrogels, and the plate was transferred into the incubator. The medium was changed every 4 days.

3.4.8 Live/Dead Assay

Spheroids' viability was investigated using a live/dead assay kit (Thermo Fisher Scientific Inc., Waltham, MA, USA). Briefly, the activity of intracellular esterase induces non-fluorescent, cell-permeant calcein acetoxymethyl ester to become fluorescent after hydrolysis, giving a green fluorescence to the viable spheroids. On the other hand, ethidium homodimer only enters and binds to nucleic acids into damaged cells, producing a red fluorescence indicating dead cells. The assay was performed at three-time points to monitor the viability of the spheroids during their growth. In detail, the medium was

removed from the plates containing the spheroids-embedded hydrogels, and the samples were washed twice with PBS. A phosphate buffer solution containing calcein and ethidium homodimer was then added, and the plate was kept in incubation at 37 °C for 1 hour. Finally, the solution was replaced with fresh PBS before imaging the samples under a Fluorescence Microscope (EVOS FLoid Cell Imaging Station, ThermoFisher, Waltham, MA, USA).

4. Results and discussion

4.1 Invasomes synthesis and characterization

The Invasomes were prepared following the recipe reported in the experimental section. The appearance of a cloudy suspension upon addition of water to the alcoholic lipid solutions visually confirmed the formation of the vesicles that, after the overnight stirring and the dialysis process, were characterized to determine the size, morphology, stability, and encapsulation efficiency of the fluorescent tracer and the prodrug.

4.1.1 Encapsulation efficiency of Rhodamine

To load Rhodamine into the Invasomes, a feeding solution of the fluorophore dissolved in Ethanol (30 μL 2 mM) was used. The resulting EE of the Invasomes was close to 81.00 ± 0.15%, corresponding to a Rhodamine concentration equal to 3.2 mg/mL of sample.

The encapsulation of rhodamine as a fluorescent label allowed the studies of the penetrability of the nanovesicles in cells and in the skin.

4.1.2 Encapsulation efficiency of 5-ALA

To encapsulate 5-ALA, multiple conditions were investigated to optimize the preparation and obtain the best encapsulation efficiency. Several parameters were considered, such as the stirring time, the addition of a sonication step, and the use of a pH gradient.

By using a pH gradient, the best encapsulation efficiencies were obtained. Moreover, by varying the feeding concentration of the drug, a curve of EE of the samples versus the initial concentration of 5-ALA was set. The loading capacity (LC) of the nanovesicles was estimated as well.

Figure 4.1 reports the EE and LC versus the feeding concentration of 5-ALA. It can be observed that by increasing the feeding concentration from 54 μg/mL to 1667 μg/mL, the EE decreases being the maximum value close to 60 % when the feeding concentration is equal to 54 μg/mL and reaching 10% when the feeding concentration is 1667 μg/mL. This suggests that the nanovesicles reached the loading saturation. To

confirm this hypothesis, the loading capacity, which is the mass of drug encapsulated per mass of sample, was calculated, and its variation according to the feeding concentration was analyzed. Figure 4.1 (B) shows a logarithmic trend confirming that the nanovesicles have a loading capacity limit between 100 and 120 μg of drug per mg of sample. This establishes a limit of feeding concentration of 833 μg/mL of ALA from which there is no benefit to rising. At this feeding concentration, the EE is 24%.

Comparing the values of EE obtained in this work with the ones found in the literature, the values achieved are slightly lower. For instance, Zhang, Z. *et al.* produced phosphocholine-based nanovesicles using pH gradient active loading to encapsulate 5-ALA and got an EE of 51% (Zhang, et al., 2016). The value of EE attained in the present work for the same feeding concentration was 10%. Since Zhang, Z. *et al.* used a very similar protocol, this indicates there is still the possibility to further optimize our methods.

Other authors, such as Lin, M. *et al.* Bragagni, M. *et al.,* and Li, A. *et al*., encapsulate 5-ALA in lipid-based nanovesicles through the film hydration method (Lin, et al., 2016) (Liy, et al., 2021) (Bragagni, et al., 2015). In the case of Lin, M. *et al.* work, an EE value of around 15% was achieved, in turn, in the present work and for the corresponding feeding concentration, the value of EE was less than 10%. Bragnani, M. *et al.* also accomplished outstanding EE values using the thin film hydration method and with the reverse phase evaporation technique. These results make the thin film hydration and phase evaporation methods worth to explore.

Finally, Luan, S. *et al.* used the ammonium sulfate gradient method for the same purpose and got an EE of 31,5%, in this work, for the correspondent feeding concentration, the EE was 42% (Luan, et al., 2021). Thus, this method is not in the future perspectives to reach better EE values.

Appendix 1 resumes the data found and shows the comparison between EE in the literature versus the one obtained for the correspondent feeding concentration of 5-ALA.

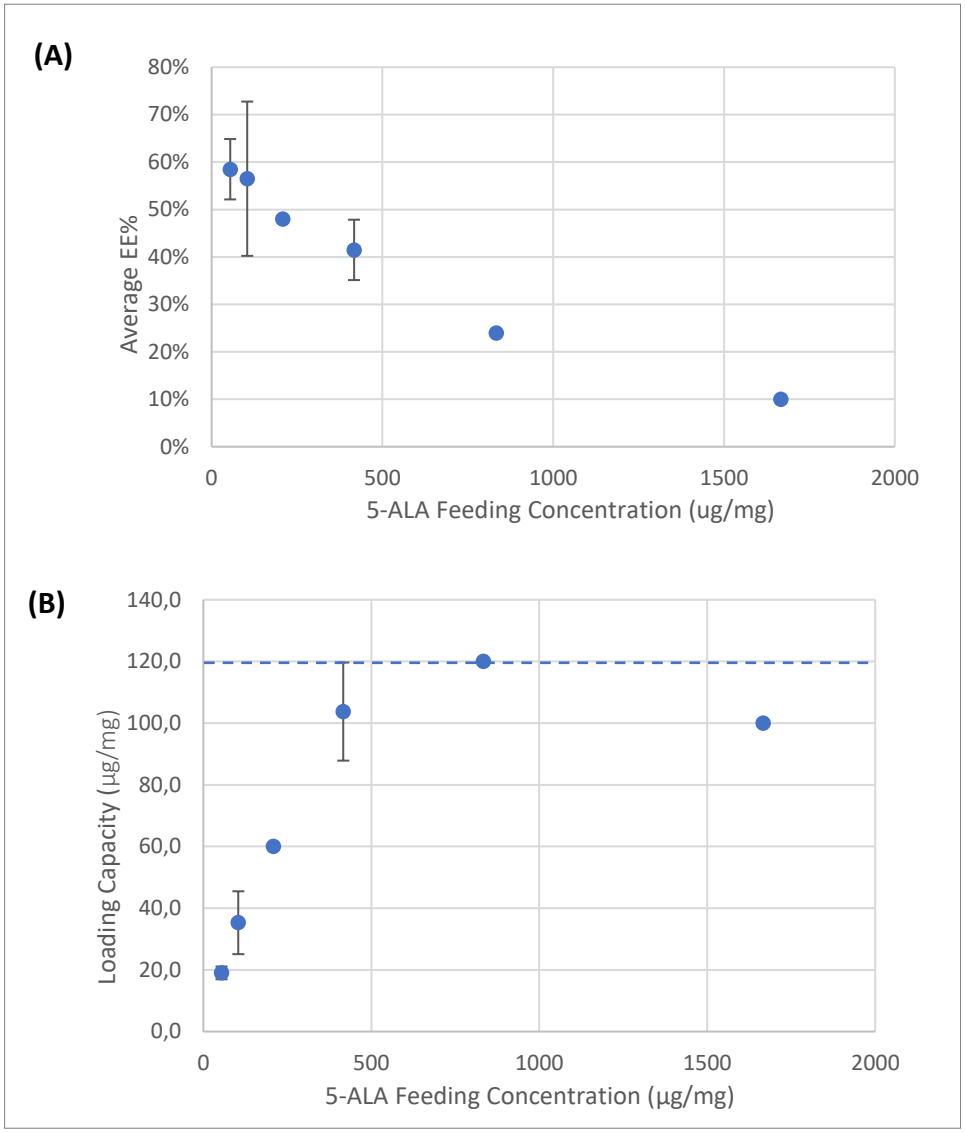

Figure 4.1 – (A) 5-ALA Encapsulation efficiency curve and (B) Loading capacity versus the feeding concentration

4.1.3 Morphological characterization

The size and morphology of empty Invasomes (Empty INV), Invasomes loaded with 5-ALA (ALA INV), and Rhodamine (RHOD INV) were analyzed through DLS and TEM.

It is known that the size of the drug delivery system influences its stability, EE, drug release profile, bio-distribution, and cellular uptake (Danaei, et al., 2018). For transdermal applications, lipid nanoparticles with 300 nm or less can deliver their content into the deeper layers of the skin to some extent, but only with 70 nm or below has been shown maximum efficiency in the delivery in both dermal and epidermal layers (Danaei, et al., 2018) (Despotopoulou, et al., 2021). Thus, in this work, a goal of reaching nanovesicles with less than 200 nm was set.

Concerning the DLS data presented in Figure 4.2 and Table 4.1, the average hydrodynamic size of Empty INV, ALA INV, and RHOD INV were 202,4 ± 2,7 nm, 154,8 ± 18,8 nm, and 196,5 ± 7,6 nm, respectively. Since they are all 200 nm or less, their size is according to what was expected.

The nanovesicles with 5-ALA look smaller compared to the other types of nanovesicles. This effect could be due to the electrostatic interactions between the entrapped 5-ALA in its protonated form and the negatively charged phospholipids, resulting in a contraction of the whole vesicle. This behavior has already been described by (Pierre, et al., 2001).

Furthermore, the nanocarriers smaller than 150 nm can enter or exit fenestrated capillaries in the tumor microenvironment or liver endothelium, so ALA INV's size likely enables such a transport process (Danaei, et al., 2018).

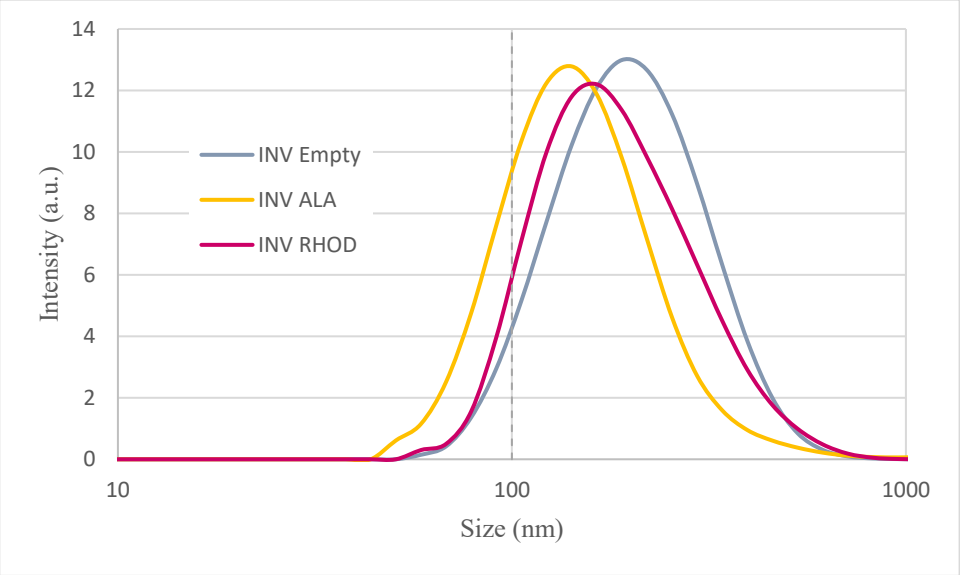

Figure 4.2 - Average size distribution of Empty INV, ALA INV, and RHOD INV

The polydispersity index (PDI) estimates the size distribution of a sample, a crucial parameter for a nanosystem designed for drug delivery. In the case of lipid-based particles, it is commonly considered acceptable a PDI below 0.3, indicating a monodisperse sample (Danaei, et al., 2018). According to the collected data, the samples have a PDI between 0.2 and 0.3, evidencing a good degree of monodispersion, thus indicating that they are suitable for the delivery purpose.

Morphological analysis by TEM imaging (Figure 4.3) shows that the empty vesicles are rounded with an average size of 50 nm (Figure 4.3 a). Those loaded with Rhodamine look hairy and smaller (size close to 45 nm), while the particles loaded with 5-ALA are more irregular and slightly larger with an average size close to 58 nm and broad size distribution (the standard deviation indeed is ±15 nm) (Figure 4.3 b-c). This size and morphological variation can be associated with the presence of the load and its interaction with the phospholipids. 5-ALA, for instance, is a hydrophilic compound. It is expected to accommodate inside the vesicle's core, thus providing some physical resistance to the contraction that happens when the sample is dried for TEM analysis (Zacheo, et al., 2020). As a general comment, the TEM size of all samples is much smaller than that measured by DLS. This effect is not surprising as the DLS measures consider the hydrodynamic diameter of the samples, while for TEM imaging, the vesicles are dried on the grid, thus losing the internal water volume. Table 2 reports the sizes, the PDI, and the surface charge of the three types of vesicles, evidencing the apparent discrepancy between the TEM and the DLS measures.

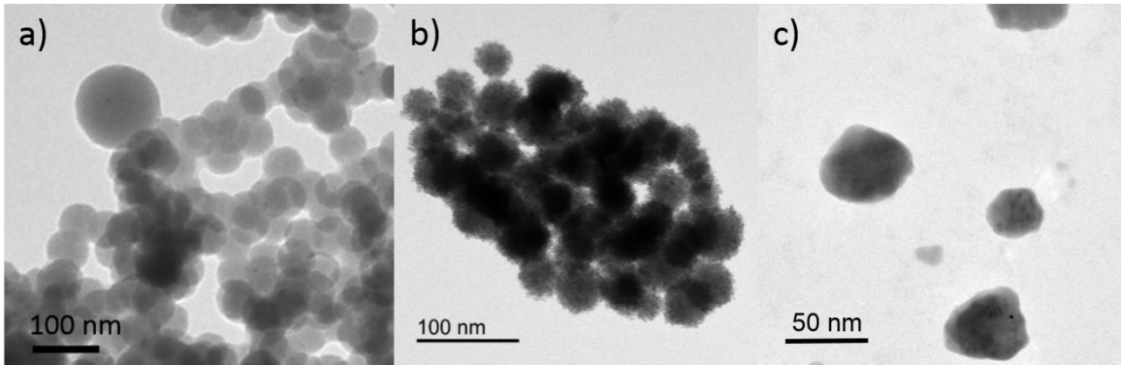

Figure 4.3 – TEM images of a) empty Invasomes, Invasomes loaded with b) Rhodamine, and c) 5-ALA.

Table 4.1 - DLS and TEM data from Empty INV, ALA INV, and RHOD INV.

Particle	TEM size (nm)	DLS size (nm)	PDI	Surface charge (mV)	Size stability
Empty NV	50,8 ± 7,4	202,4 ± 2,7	0,221 ± 0,1	- 14,4 ± 1,9	Measured up to 15 days
ALA NV	53,7 ± 15,0	154,8 ± 18,8	0,318 ± 0,1	-18,3 ± 2,5	Measured up to 20 days
Rhod NV	44,9 ± 3,7	196,5 ± 7,6	0,215 ± 0,1	-24,8 ± 11	Measured up to 20 days

4.1.4 Invasome's stability over time

To monitor the stability of the nanovesicles over time, the surface charge and the hydrodynamic diameter were measured at defined time points.

The measure of the Zeta Potential is of great importance to confer stability since a ZP above ± 30 mV suggests that the dispersion of nanovesicles would not suffer aggregation due to electrostatic repulsion between particles of the same charge (Niaz, et al., 2022). The ZP also plays an important role in predicting the initial adsorption of nanoparticles onto the membrane of the cell.

According to the data reported in Table 4.1, the ZP of the Empty INV, ALA INV, and RHOD INV are -14,4, -18,3, and -24,8 mV, respectively, at physiological pH, a ZP between +10 and -10 mV is considered to be neutral, so it is possible to assume that the charge of Empty INV almost neutral, making these particles susceptible to aggregation. The charge of ALA INV and RHOD INV is more negative, thus expected to be more stable (Clogston & Patri, 2011).

Moreover, the charge is a major determinant in the interactions between nanoparticles and cells (Cui, et al., 2018). It is commonly accepted that a particle with a positive charge interacts and is internalized faster than a negatively charged particle due to the negative charge of the cell membrane. (Cui, et al., 2018). This phenomenon has already been reported by several research groups (Blanco, et al., 2015).

Furthermore, positively charged vesicles tend to be sequestrated by macrophages and be accumulated in the lungs, liver, and spleen. In contrast, negatively charged particles have shown longer circulating half-lives and less accumulation in these organs, which translates into better accumulation in tumors (Blanco, et al., 2015) (Yamamoto, et al., 2001). The information gathered leads to the conclusion that for effective nanoparticle delivery to tumors, the particles should be neutral or slightly negative while in the intravenous system but switch to a positive charge when they enter the tumor microenvironment (Blanco, et al., 2015). This concept boosted innovative strategies for charge-switching nanoparticles in response to environmental stimuli, such as pH, which is very useful for tumor delivery because the tumor microenvironment is more acidic (Blanco, et al., 2015) (Yuan, et al., 2012).

In the specific case of transdermal delivery, it is reported that positively charged nanoparticles have more success than negatively charged particles in crossing the *stratum corneum*, which is negatively charged (Despotopoulou, et al., 2021).

According to this information, the three kinds of particles produced, being neutral and slightly negative, will probably have a good half-life if circulating inside a body, but possibly won't be the most successful particles in entering inside the cells or passing through the *stratum corneum*. Therefore, one of the following steps could be the functionalization of the surface of the vesicles with positively charged chemical moieties.

The stability of each type of nanovesicle was also studied by measuring the size and PDI of the particles over time using the DLS. In the meantime, the samples were kept in the fridge at 4°C.

The variation of the particles' size over time can alter its predicted performance. These variations must be considered when developing encapsulated therapeutic agents, being the optimal scenario a constant and narrow size distribution (Danaei, et al., 2018). Phenomenon such as agglomeration and dissolution can also affect the toxicity of the particles, and the dynamic size distribution should be evaluated. Changes in this characteristic over time can be caused by the collisions between particles (Vijver, et al., 2018).

Figure 4.4 shows the variation of the average size over time of Empty INV, RHOD INV, and ALA INV. There is a decrease in the size in all three samples, so it's possible to assume that no aggregation occurs. In the RHOD INV and ALA INV samples, the size decreases until day 15 and then stabilizes. ALA INV has the smallest decay in size but has the higher standard deviation values.

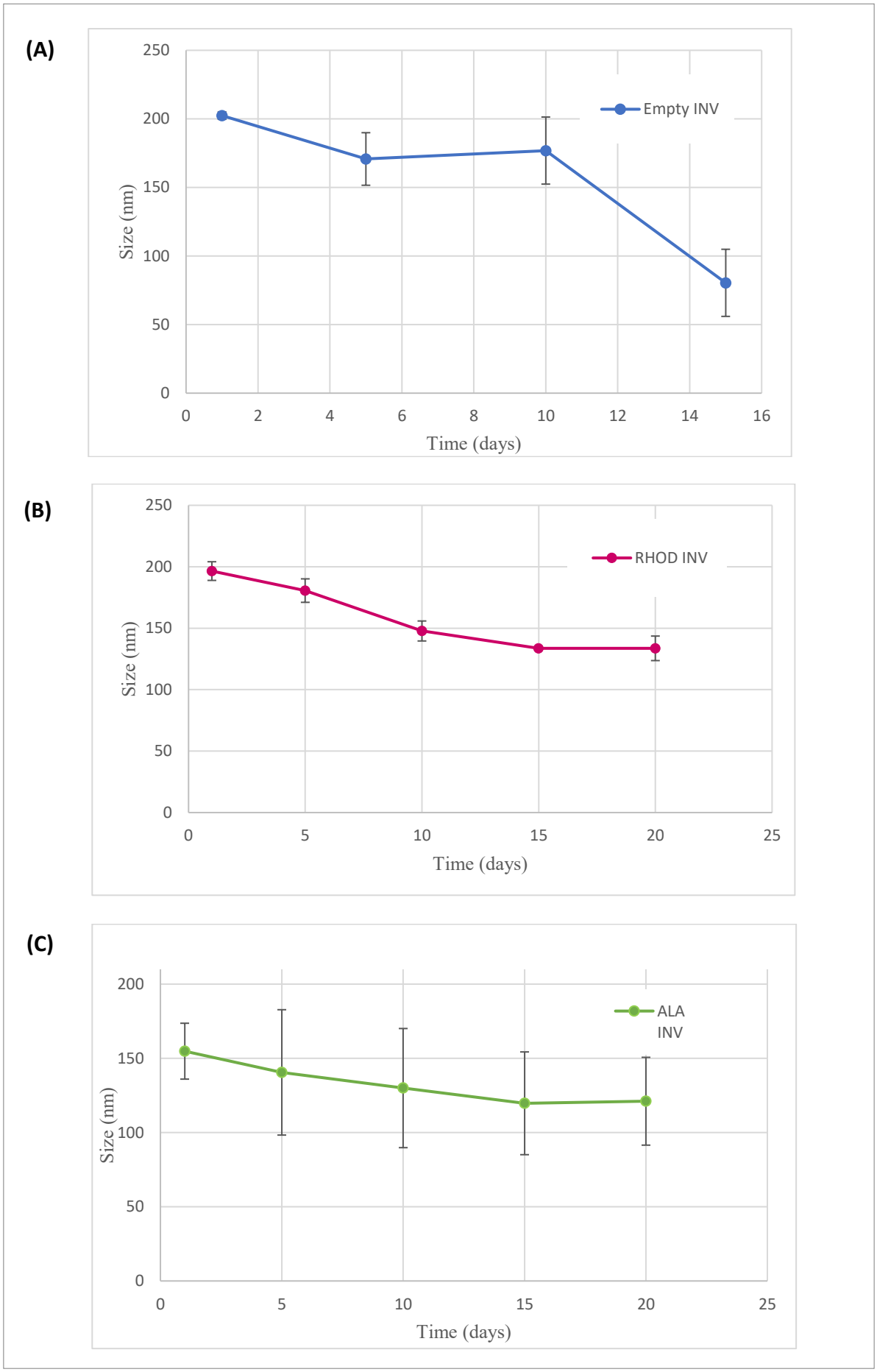

Figure 4.4 - Variation of size over time of (A) Empty INV, (B) RHOD INV, and (C) ALA INV.

Concerning the PDI values, they look to increase over time for the three samples, thus evidencing that the size reduction of the particles is associated with a general increase in the sample's size distribution due to the simultaneous presence of species with different sizes (Figure 4.5).

This behavior has already been reported in the literature (Ballell-Hosa, et al., 2022). Indeed, even in this recent work, the sizes of the nanovesicles decreased during the first week and then stabilized, accompanied by an increase in the PDI values. The authors suggest that the tendency for size reduction is related to the thermodynamic aspects of the vesicles since particles minimize the free energy with the formation of smaller and more energetically stable vesicles.

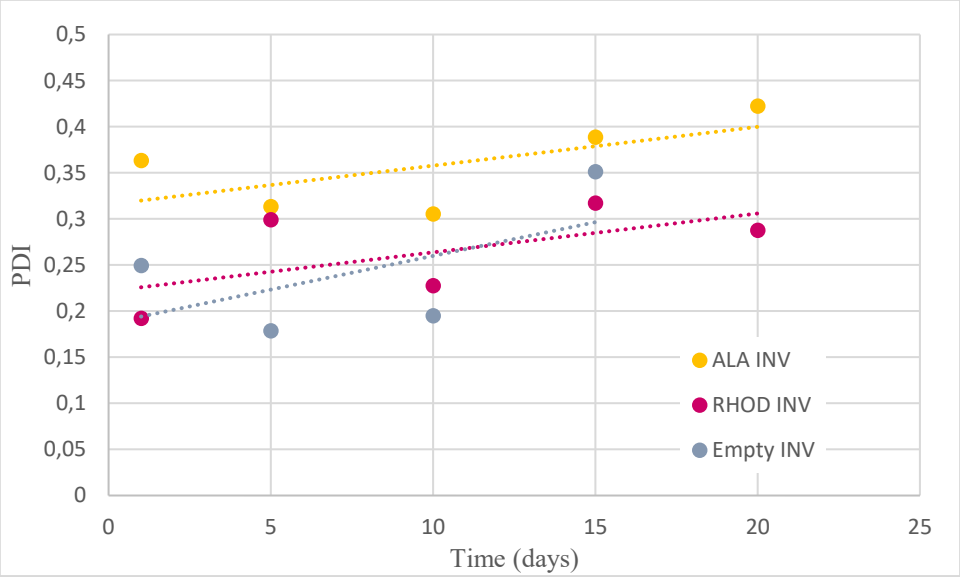

Figure 4.5 - PDI over time of Empty INV, RHOD INV, and ALA INV

4.1.5 Thermostability

The thermal stability of the samples was determined by TGA measures of the Empty INV and ALA INV. The TGA curves and their first derivatives to better evidence the steps in the weight loss are reported in Figure 4.6.

The first slight decrease around 100°C corresponds to the loss of water residues. Around 300°C, there is a significant decrease in the mass of the samples due to their decomposition. Both samples show very similar behavior, though the vesicles with 5-

ALA display degradation at a slightly higher temperature, likely due to the interactions between 5-ALA and the phospholipids.

This thermal behavior evidences a good thermostability of the nanovesicles.

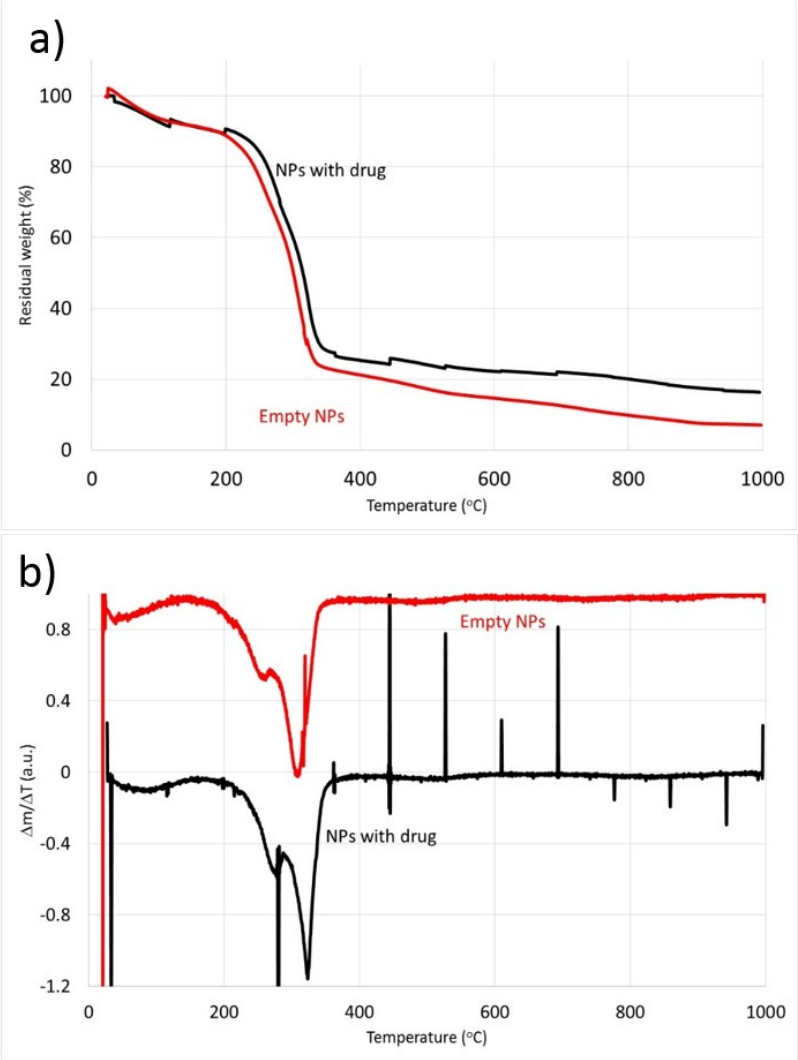

Figure 4.6 – a) TGA curves and corresponding b) first derivatives of the Empty INV (red curve) and ALA INV (black curve)

4.1.6 Diffusion of the Invasomes into *ex-vivo* skin

A prelaminar study of the diffusion of the ALA INV was done with a lab-made apparatus that mimics a Franz diffusion cell. In this set of experiments, Invasomes loaded with Rhodamine encapsulated (RHOD INV) were used to enable the visualization of the particles and their diffusion through the skin. The apparatus containing a disk of pig skin was prepared as reported in the experimental section. The decrease of the

photoluminescence signal of both the RHOD INV sample and the solution of free Rhodamine, previously added over the skin, was monitored over time.

The curves of Figure 4.7 show that the diffusion profiles of the RHOD INV and free Rhodamine are similar, reaching. 30-40% of the fluorescence decay compared to time 0 within the first hour. After 2 and 4 hours, around 60% and 80% of the signal decays due to skin penetration. Table 4.2 reports the values of the percentage variation of the fluorescence intensity for both types of samples over time.

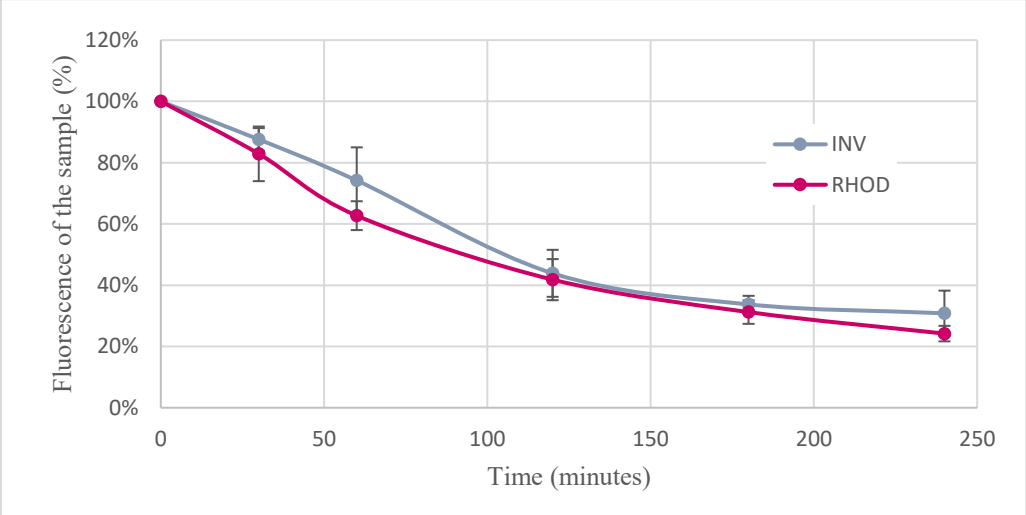

Figure 4.7 - Fluorescence percentage over time of the RHOD INV and free Rhodamine samples incubated on the *ex-vivo* pig skin

Table 4.2 - Fluorescence percentage variation over time of the RHOD INV and free rhodamine samples incubated with the ex-vivo pig skin

Time (minutes)	INV RHOD (%)	Free Rhodamine (%)
0	100	100,0
30	88 ± 4	83 ± 9
60	74 ± 11	63 ± 5
120	44 ± 8	42 ± 7
180	34 ± 3	31 ± 8
240	31 ± 7	24 ± 2

The images acquired with the fluorescence microscope (Zeiss Azio Zoom) (Figure 4.8) confirm the capability of the nanovesicles to diffuse through the pig skin and penetrate some hundreds of microns after 4 hours of incubation. Indeed, the images show the transversal section (Figure 4.8 a-b) and the upper view (Figure 4.8 c-d) of the skin

samples after incubation. The high fluorescence signal is also noticeable in the upper view images due to the accumulation of particles.

On the other hand, no fluorescent signal can be detected in the control skin pig (Figure 4.8 e-f).

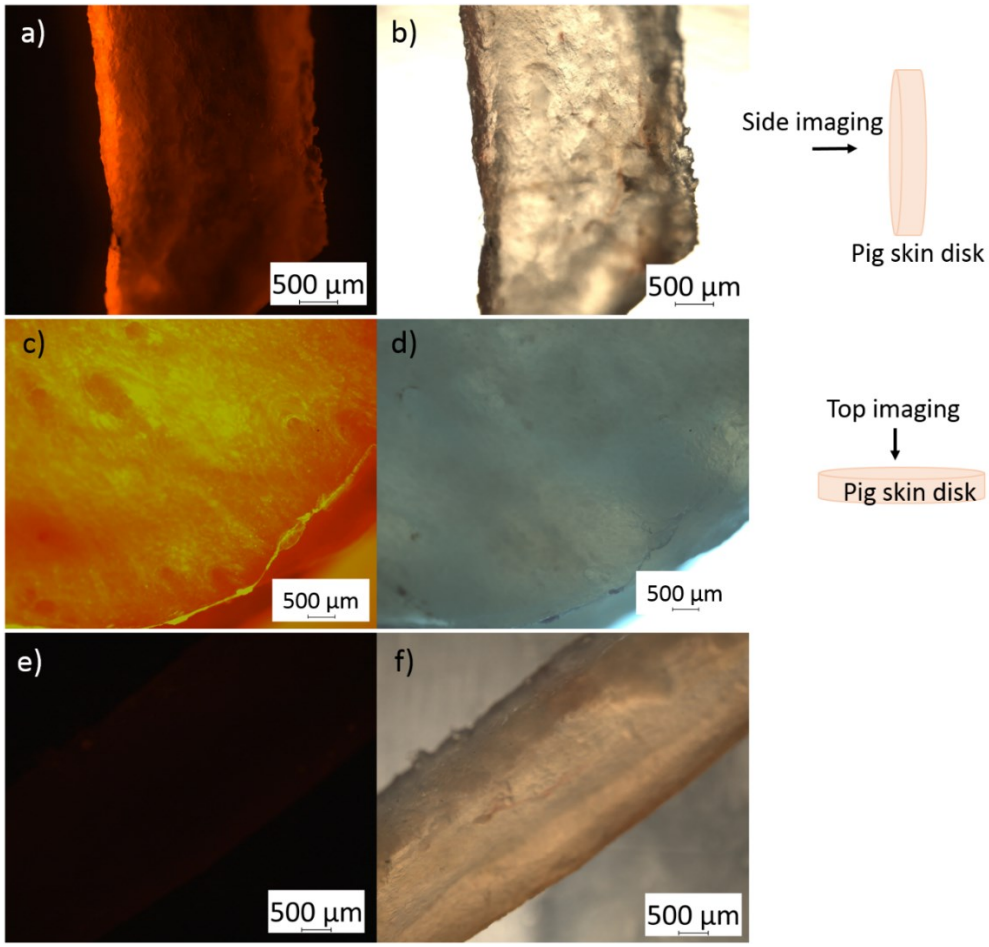

Figure 4.8 – a-b) Images of the side-view of the *ex-vivo* pig skin after 4 hours incubation with RHOD INV samples; c-d) Images of the top-view of the *ex-vivo* pig skin after 4 hours incubation with RHOD INV samples; e-f) Images of the side view of the control pig skin (without the addition of the nanovesicles)

These preliminary studies evidence the potential use of these nanovesicles as tools for transdermal delivery of molecules and drugs.

4.2 Cellular tests

4.2.1 Cytocompatibility of Single phospholipid-made vesicles

At the beginning of this thesis work and with the attempt to define the cytocompatibility of the nanovesicles developed herein, single lipids nanovesicles were prepared, characterized, and tested. Though this part has not been included in the work, it is worth mentioning the results of the MTT assay performed with three different cell lines, HBL, HaCat, and MCF7. The cells were administered with different concentrations of the single phospholipids-made nanovesicles, and the IC_{50} was evaluated after 24 h incubation. The half-maximal inhibitory concentration (IC_{50}) is the concentration of the nanovesicles needed to inhibit cell viability by 50%.

Table 4.3 - Presentation of the single phospholipids-made vesicles and IC50 values of HBL, HaCat, and MCF7 cells incubated with them

Lipid	Length of the alkyl chain	IC_{50} HBL (μg)	IC_{50} HaCaT (μg)	IC_{50} MCF7 (μg)	DLS size (nm)
DLPC 12	C12	287 ± 22	302 ±1	386 ± 3	500
DSPE	C13	183 ± 14	167 ±6	72 ± 1	1500
DMPC	C14	763 ± 66	794 ± 12	910 ± 17	140
DLPC 14	C14	1044 ± 97	1091 ± 43	1222 ± 98	1000
Lecithin	C15	803 ±61	595 ± 25	869 ± 81	320

Nanovesicles composed of either DLPC 12C, DLPC 14C, DSPE, DMPC, Lecithin, or CisPC were respectively prepared. The size of the vesicles is reported in the last column of Table 4.3, showing that DMPC and CisPC produce small vesicles (around 140 nm diameter) compared to those prepared with DSPE and DLPC 14C, that show an average diameter larger than 1 μm. An intermediate diameter is reported or those made of DLPC12 and Lecithin.

The IC_{50} values show that shorter the alkyl chain (C12 and C13) lowers the cytocompatibility of the nanovesicles. Interestingly, the results obtained with the three cell lines are comparable and evidence that DLPC14-based vesicles are the most biocompatible. Consequently, the phospholipids with longer alkyl chains (C14 and 15) were chosen as components of the lipid mixture of the nanovesicles.

4.2.2 Delivery of ALA and Photodynamic therapy in melanoma cells

To study the ALA INV's therapeutic potential and the photodynamic treatment response, cellular tests were performed with HBL and Hacat cells that, upon seeding into the well plates, were administered with either free ALA, Empty INV, or ALA-INV. The feeding concentration was set at 25 µg/mL in accordance with previous reports (Li, et al., 2019). After 3 h incubation, the medium was removed, the cells washed, and a thin film of PBS was added prior to applying the red lamp (excitation wavelength at 630 nm) for 15 minutes of irradiation. Soon after, the cells were washed and prepared for two different assays accordingly.

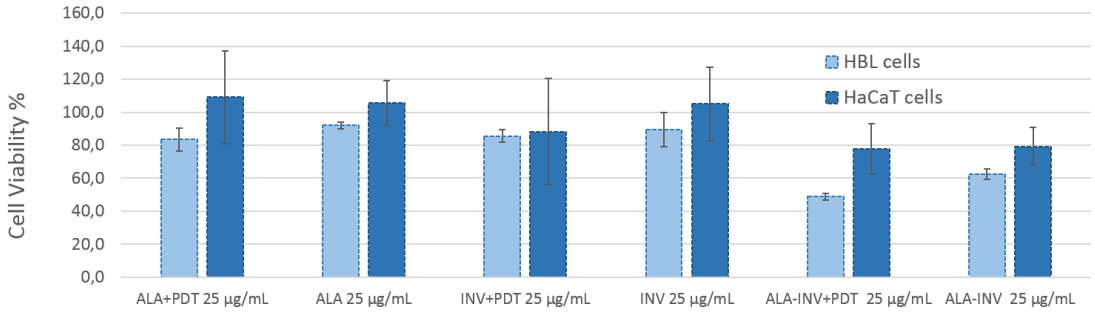

Figure 4.9 - MTT assay of HBL and HaCat cells administered with free ALA; Empty INV and ALA INV for 3 h and assayed after 24 h, respectively. In addition, the effect of the photodynamic treatment (+PDT) was analyzed.

In the case of the MTT assay, fresh medium was added, and the effect of the vesicles on the cellular viability was assayed 24 h later. The results are reported in Figure 4.9, showing that the empty vesicles are well tolerated by both types of cells, with viability values higher than 85%. The treatment with free ALA was less effective, even upon application of the photo treatment. Indeed, the viability reaches values higher than 80% after ALA incubation and PDT. On the other hand, when the cells were incubated with ALA-INV the cell viability dropped to less than 50% and to around 78%, in the case of HBL and HaCat cells, respectively. Thus, it looks like cells respond to the combined treatment upon metabolization of 5-ALA to PpIX. In particular, melanoma cells (HBL) seem to be more sensitive to the treatment than HaCat cells. Noteworthy, the ALA-INV without light irradiation induces a reduction of the cell viability: it looks that the 5-ALA delivered by the nanovesicles is able to exert an effect, likely at the mitochondria, as the assay is based on the evaluation of enzymatic response in this organelle. These results deserve further investigation in future tests.

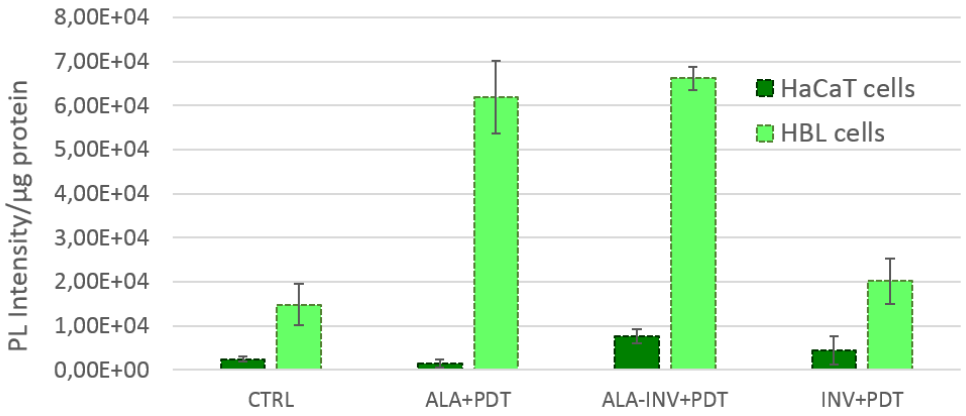

Figure 4.10 - DCF assay of HBL and HaCat cells administered with free 5-ALA; Empty INV and ALA INV for 3 h and subjected to the light treatment for 15 minutes.

In the case of the DCF assay, the cells were immediately processed to detect the generation of ROS species after the light treatment.

As shown in the histograms of Figure 4.10, the combined treatment of the cells with 5-ALA, either free or encapsulated and PDT provoke a strong ROS generation only in HBL cells. This effect is 3 times higher than in the cells administered with Empty INV.

This data is confirmed by the fluorescent images of the cells after the DCF assay. Indeed, a bright fluorescent green signal can be detected in HBL cells treated with 5-ALA (Figure 4.11). The fluorescent cells also look rounded, a clear sign of cellular sufferance, detachment from the substrate, and propensity to die. On the other hand, a negligible fluorescent signal can be detected in HaCat cells (Figure 4.12).

These findings demonstrate the potential use of the vesicles as delivery systems and mediators of the oxidative effect of the drug. Further tests will be performed to clearly understand the internalization process of the Invasomes and shed light on the intracellular effects of the combined treatment.

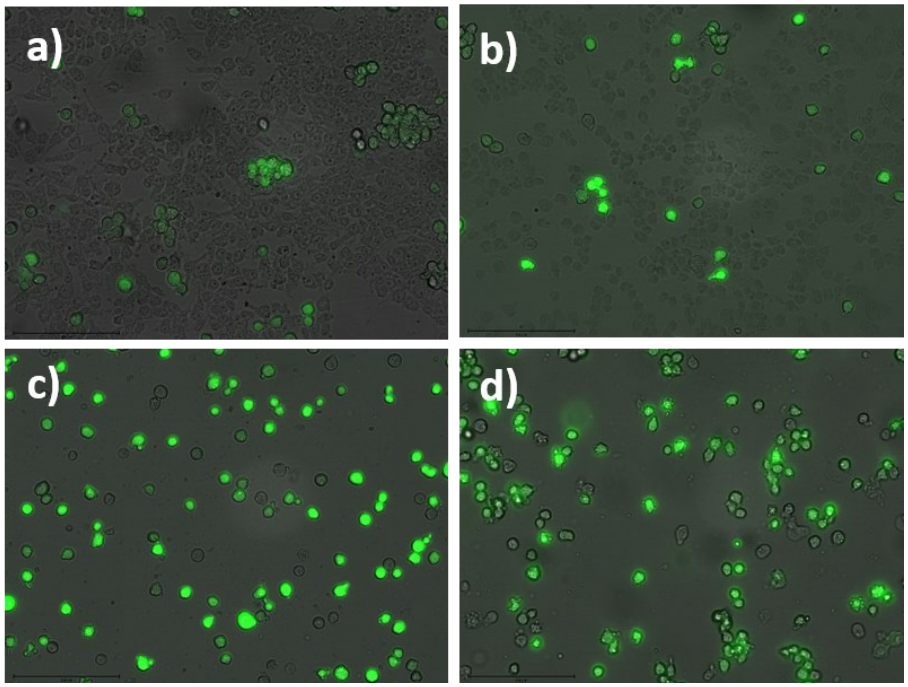

Figure 4.11 - Qualitative analysis of the DCF assay showing HBL cells: a) control sample; cells incubated with b) Empty INV, c) free ALA, and d) ALA-INV for 3 h and after 15 minutes of light irradiation.

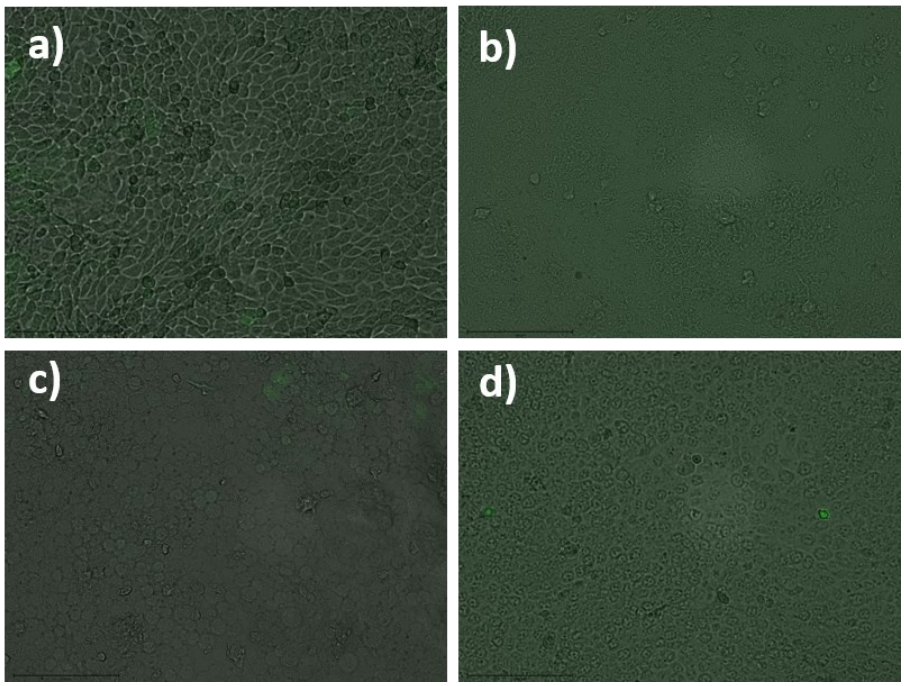

Figure 4.12 - Qualitative analysis of the DCF assay showing HaCat cells: a) control sample; cells incubated with b) Empty INV, c) free ALA, and d) ALA-INV for 3 h and after 15 minutes of light irradiation.

4.2.3 Development of agarose-collagen hydrogel to host melanoma spheroids

The aim of this part of the thesis work is to develop a hydrogel that resembles the 3D skin tumor. Indeed, the hydrogel is designed to encapsulate and sustain melanoma tumor spheroids' growth and facilitate the adhesion and proliferation of keratinocytes over the surface, as illustrated in Figure 4.13. To this aim, several collagen formulations were tested, and preliminary studies were performed to assess the capability of the collagen formulations to host the tumor growth and to allow the adhesion of the keratinocytes. Furthermore, studies to evaluate the differences between collagen from different origins, namely bovine Type I collagen and Nile Tilapia Type I collagen, were conducted, but they didn't lead to conclusive nor satisfactory results (Appendix A).

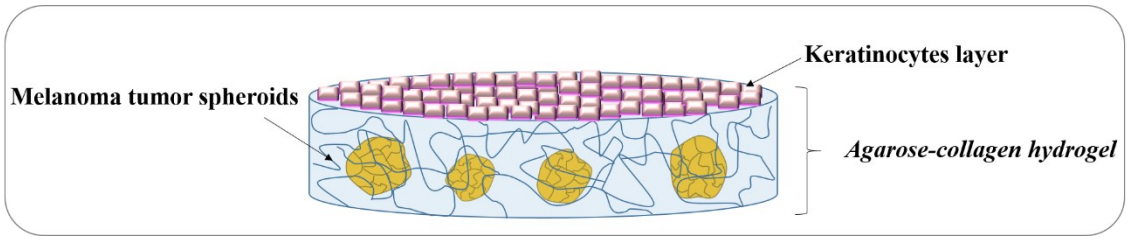

Figure 4.13 - Sketch of the 3D skin tumor model

Here are reported the results obtained with the formulation that provided the most promising features. The 3D skin tumor model proposed is made of a hosting hydrogel composed of an agarose-collagen blend that encapsulates HBL tumor spheroids. Upon gelation, keratinocytes cells were deposited on the hydrogel. The cell growth was monitored over time. Figure 4.14 reports the Z-stack acquisition of different planes of the agarose-collagen hydrogel. The upper plane shows the keratinocytes arranged to form a monolayer covering the surface of the hydrogel. By moving through lower Z-planes the melanoma spheroids are visible.

Upon the formation of a keratinocyte monolayer and the growth of the melanoma spheroids, preliminary studies to evidence the nanovesicle diffusion through the hydrogel were performed.

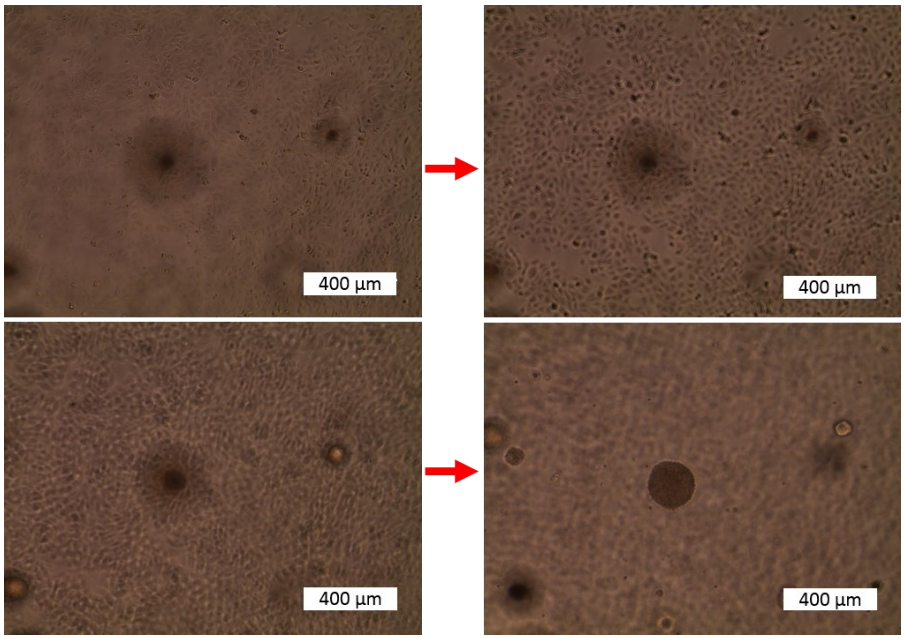

Figure 4.14 – Series of 4 images taken at different z-planes of the agarose collagen hydrogels embedded with the melanoma cells and covered by a layer of keratinocytes after 7 days of growth

4.2.4 Penetration of the Nanovesicles through the agarose-collagen hydrogels to the melanoma spheroids

RHOD INV was added to the cell culture medium, and after 24 h the spheroids were fixed with paraformaldehyde and the nuclei of the cells stained with DAPI.

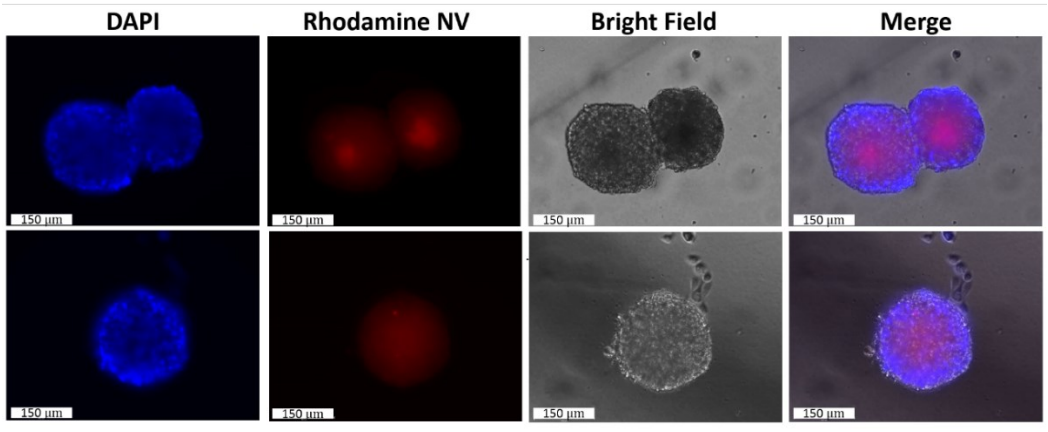

Figure 4.15 – Images of the melanoma spheroids embedded into the agarose-collagen and incubated with the RHOD-INV for 24 h. The cells' nuclei were stained with DAPI.

The images in Figure 4.15 show the fluorescent blue signal associated with the nuclei staining and the fluorescent red signal derived from the RHOD INV that, after diffusion through the hydrogel, has been internalized by the cells.

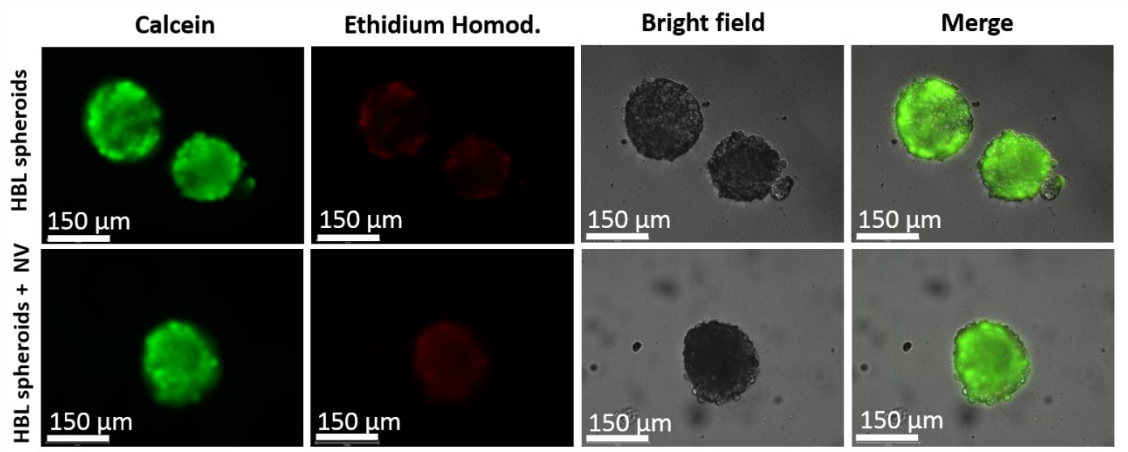

Figure 4.16 – Live/dead assay of the melanoma spheroids embedded into the agarose-collagen incubated with the Empty INV for 24h. The fluorescent green channel corresponds to the calcein signal while the red one to Ethidium Homodimer.

Furthermore, to assess the cell viability of the melanoma spheroids grown into the hydrogel and administered with the EMPTY INV, the live/dead assay was performed. Figure 4.16 shows the fluorescent images of the spheroids (control HBL spheroids in the upper panels, HBL spheroids incubated with the vesicles in the lower panels, respectively). The bright green fluorescence of calcein and the weak red signal of Ethidium Homodimer of both types of spheroid samples evidence the good biocompatibility of the vesicles.

Future studies will be conducted to evaluate the delivery capability of 5-ALA through the layer of keratinocytes and the hydrogel, and the response to the photodynamic treatment of the embedded tumoroids.

5. Conclusion

In summary, in this thesis work, phosphocholine vesicles loaded with 5-ALA were assembled and tested as delivery vectors. The best properties, such as size and EE, were achieved with the protocol that included the solvent injection method and pH gradient active loading. The EE and LC were studied, and a feeding concentration of 833 μg/mL of 5-ALA reached the limit of the vesicle's LC. At this feeding concentration, the EE was 24%.

The ALA INV vesicles had an average diameter of 154.8 ± 18.8 nm, and by analyzing the size over time, this value decreased until day 15, when it stabilized. The PDI values slightly increased over time, thus evidencing a general increase in the size distribution. According to the TGA results, both ALA INV and Empty INV had good thermostability.

Prelaminar studies of the diffusion of ALA INV into ex vivo pig skin showed that the vesicles could penetrate the skin, thus demonstrating their potential for transdermal delivery.

Regarding the 2D cellular tests, firstly was possible to conclude that DLPC 14 and lipids with a longer alkyl chain had higher values of cytocompatibility, being the first candidates chosen to be part of the composition of the nanovesicles.

The results achieved in the 2D cellular tests to assess the cytotoxic potential of the ALA INV towards skin cancer cells demonstrated that empty vesicles were well tolerated by cells having reached viability values higher than 85%. Free 5-ALA, with or without photodynamic treatment, did not show to be effective. In turn, ALA INV proved to be effective, especially in HBL cells. Even without the photodynamic treatment, ALA INV caused a reduction in cell viability, possibly evidence of 5-ALA being delivered to the cells and enzymatically converted in PpIX. These results need to be further investigated to reach more robust conclusions.

Complementing the cytotoxicity tests, the results of the DCF assay indicated a higher production of ROS species in the HBL cells, corroborating with the lower viability observed after ALA INV treatment, demonstrating the potential of these nanovesicles as delivery systems and as mediators of the oxidative effect of 5-ALA.

The assembly of the 3D melanoma spheroids in the agarose-collagen hydrogel covered by a layer of keratinocytes was successfully achieved. It is worth noting that

initially, human basal carcinoma cells were considered for the tumor spheroids and the 2D tests, unfortunately, the cell's very slow replication time was incompatible with the timing predicted for the studies intended to carry out.

The cellular test done with the 3D model developed to evaluate the diffusion of the Invasomes through the tumor spheroids demonstrated that the vesicles were able to cross the hydrogel and enter the spheroids effectively. According to the live/dead assay, after 24h of incubation with Empty INV, evidence of good biocompatibility was achieved.

6. Future perspectives

As future perspectives, although the EE values obtained were satisfactory, according to the literature found, there is still the opportunity to further optimize the protocol of 5-ALA loading in order to reach higher EE values.

In the skin diffusion studies, it would be very interesting to use human skin samples, and further optimize the setup created for this test.

Regarding the cellular tests, further investigation is needed to clearly understand the internalization process and the intracellular effects of the ALA INV with and without photodynamic treatment.

Relatively to the tests in the 3D skin cancer model, evaluation of 5-ALA delivery through the keratinocyte layer and the hydrogel has to be done, as well as the study of the efficacy of INV ALA treatment with and without photodynamic treatment in the embedded tumoroids.

Additionally, to complete this work, the development of a cream formula to help the topical administration of the treatment must be accomplished.

Finally, when is reached the point of having robust evidence that this treatment is efficient, effective, and safe, the next step will be tests on human skin samples.

7. References

Abd, E., Yousef, S., Pastore, M. & al, e., 2016. Skin models for the testing of transdermal drugs. *Dovepress - Clinical Pharmacology: Advances and Applications,* Volume 8, p. 163–176.

Akash, M. & Rehman, K., 2020. Thermo Gravimetric Analysis. In: *Essentials of Pharmaceutical Analysis.* Singapore: Springer.

Ballell-Hosa, L., González-Mira, E., Santana, H. & al, e., 2022. DELOS Nanovesicles-Based Hydrogels: An Advanced Formulation for Topical Use. *Pharmaceutics,* 14(1), p. 199.

Barenholz, Y., 2012. Doxil® — The first FDA-approved nano-drug: Lessons learned. *Journal of Controlled Release,* 160(2), pp. 117-134.

Blanco, E., Shen, H. & Ferrari, M., 2015. Principles of nanoparticle design for overcoming biological barriers to drug delivery. *Nature biotechnology,* Volume 33, pp. 941-951.

Bottom, R., 2008. *"Thermogravimetric analysis." Principles and applications of thermal analysis.* s.l.:Blackwell Publishing.

Bragagni, M. et al., 2015. Development and ex vivo evaluation of 5-aminolevulinic acid-loaded niosomal formulations for topical photodynamic therapy. *International Journal of Farmaceutics,* 494(1), pp. 258-263.

Clogston, J. & Patri, A., 2011. Characterization of Nanoparticles Intended for Drug Delivery - Zeta Potential Measurement. *Methods in Molecular Biology,* Volume 697, pp. 63-70.

Cui, Y. et al., 2018. Enhanced biocompatibility of PAMAM dendrimers benefiting from tuning their surface charges. *Materials Science and Engineering,* Volume 93, pp. 332-340.

Danaei, M. et al., 2018. Impact of Particle Size and Polydispersity Index on the Clinical Applications of Lipidic Nanocarrier Systems. *Pharmaceutics,* 10(2).

Despotopoulou, D. et al., 2021. The technology of transdermal delivery nanosystems: from design and development to preclinical studies. *International Journal of Pharmaceutics,* Volume 611.

Dianzani, C., Zara, G. & Maina, G., 2014. Drug Delivery Nanoparticles in Skin Cancers. *BioMed Research International,* Volume 2014.

Dika, E. et al., 2020. Basal Cell Carcinoma: A Comprehensive Review. *International Journal of Molecular Sciences,* 21(15).

Esmaeili, J. et al., 2021. Employing hydrogels in tissue engineering approaches to boost conventional cancer-based research and therapies. *Royal Society of Chemistry Advances,* Volume 11, pp. 10646-10669.

Flaten, G. et al., 2015. In vitro skin models as a tool in optimization of drug formulation. *European Journal of Pharmaceutical Sciences,* Volume 75, pp. 10-24.

Gallo, N. et al., 2022. Aquaponics-Derived Tilapia Skin Collagen for Biomaterials Development.. *Polymers,* 14(9).

García-Pinel, B., Alcalá, C., Rodriguez, A. & al, e., 2019. Lipid-Based Nanoparticles: Application and Recent Advances in Cancer Treatment. *Nanomaterials,* 9(4), pp. 638-661.

Instruments, L., 2022. *LS Instruments - Dynamic Scattering Light (DLS).* [Online] Available at: https://lsinstruments.ch/en/theory/dynamic-light-scattering-dls/introduction [Accessed 28 07 2022].

Jeong, W., Kwon, M., Choi, H. & Kim, K., 2021. Recent advances in transdermal drug delivery systems: a review. *Biomaterials Research,* 25(24).

Jiang, T. et al., 2020. Progress in transdermal drug delivery systems for cancer therapy. *Nano Research,* Volume 13, pp. 1810-1824.

Jiang, Y., Liu, y. & Fang, S. J. M., 2020. Gold Nanoshells Coated 5-Aminolevulinic Liposomes for Photothermal-Photodynamic Antitumor Therapy. *Journal of Nanoscience and Nanotechnology,* 20(1), pp. 1-14.

Kaszuba, M., Corbett, J., Watson, M. & Jones, A., 2010. High-concentration zeta potential measurements using light-scattering techniques. *Philosophical Transactions of the Royal Society,* 368(1927), p. 4439–4451.

Kim H, X. X., 2020. Detection of Total Reactive Oxygen Species in Adherent Cells by 2',7'-Dichlorodihydrofluorescein Diacetate Staining.. *Journal of Visualized Experiments,* Issue 160.

Kolarsick, P., Kolarsick, M. & Goodwin, C., 2011. Anatomy and Physiology of the Skin. *Journal of the Dermatology Nurses' Association,* 3(4), pp. 203-213.

Krishnan, V. & Mitragotri, S., 2020. Nanoparticles for topical drug delivery: Potential for skin cancer treatment. *Advanced Drug Delivery Reviews,* 1(153), pp. 87-108.

Łasińska, I., Zielińska, A., Mackiewicz, J. & Souto, E., 2022. Basal Cell Carcinoma: Pathology, Current Clinical Treatment, and Potential Use of Lipid Nanoparticles. *Cancers,* 14(11), p. 2778.

Lee, S., Jin, S. & Kim, Y. e. a., 2017. Construction of 3D multicellular microfluidic chip for an in vitro skin model. *Biomedical Microdevices,* 19(27).

Lin, K. et al., 2019. Advanced Collagen-Based Biomaterials for Regenerative Biomedicine. *Advanced Functional Materials Journal,* 29(1804943).

Lin, M. et al., 2016. A Formulation Study of 5-Aminolevulinic Encapsulated in DPPC Liposomes in Melanoma Treatment. *International Journal of Medical Sciences,* 13(7), pp. 483-489.

Liy, A. et al., 2021. Boosting 5-ALA-based photodynamic therapy by a liposomal nanomedicine through intracellular iron ion regulation. *Acta Pharmaceutica Sinica B,* 11(5), pp. 1329-1340.

Li, Z. et al., 2019. Robust Photodynamic Therapy Using 5-ALA-Incorporated Nanocomplexes Cures Metastatic Melanoma through Priming of CD4+CD8+ Double Positive T Cells. *Advanced Science,* 6(5), p. 1802057.

Luan, S., Tran, N., Xue, H. & Wong, H., 2021. Development of a high payload, cancer-targeting liposomes of methyl aminolevulinate for intraoperative photodynamic diagnosis/therapy of peritoneal carcinomatosis. *International Journal of Pharmaceutics,* Volume 602.

Malik, Z., 2020. Fundamentals of 5-aminolevulinic acid photodynamictherapy and diagnosis: An overview. *Translational Biophotonics,* 2(1-2).

Matei, C. et al., 2013. Photodynamic therapy in the treatment of basal cell carcinoma. *Journal of Medicine and Life,* 6(1), pp. 50-54.

Mathesa, S., Ruffnerb, H. & Graf-Hausner, U., 2013. The use of skin models in drug development. *Advanced Drug Delivery Reviews,* Issue 69-70, pp. 81-102.

Minton, A., 2016. Recent applications of light scattering measurement in the biological and biopharmaceutical sciences. *Analytical biochemistry,* Volume 501, pp. 4-22.

Niaz, T., Shabbir, S., Noor, T. & Imran, M., 2022. Active Composite Packaging Reinforced with Nisin-Loaded Nano-Vesicles for Extended Shelf Life of Chicken Breast Filets and Cheese Slices.. *Food Bioprocess Technol,* Volume 15, p. 1284–1298.

Patra, J., Das, G., Fraceto, L. & al, e., 2018. Nano based drug delivery systems: recent developments and future prospects. *Journal of Nanobiotechnology,* 16(71).

Peris, K., Fargnoli, M., Garbe, C. & al, e., 2019. Diagnosis and treatment of basal cell carcinoma: European consensus-based interdisciplinary guidelines. *European Journal of Cancer,* Volume 118, pp. 10-34.

Pierre, M., Tedesco, A., Marchetti, J. & Bentley, M., 2001. Stratum corneum lipids liposomes for the topical delivery of 5-aminolevulinic acid in photodynamic therapy of skin cancer: preparation and in vitro permeation study. *BMC Dermatology,* 1(5).

Plumb, J., 2004. Cell Sensitivity Assays: The MTT Assay. In: *Cancer Cell Culture - Methods in Molecular Medicine™.* s.l.:Humana Press, pp. 165-169.

Quarta, A. et al., 2021. Investigation on the Composition of Agarose–Collagen I Blended Hydrogels as Matrices for the Growth of Spheroids from Breast Cancer Cell Lines. *Pharmaceutics,* 13(7), p. 963.

Randall, M., J. A., Rimann, M. & Wuertz-Kozak, K., 2018. Advances in the Biofabrication of 3D Skin in vitro: Healthy and Pathological Models. *Frontiers in Bioengineering and Biotechnology,* 6(154).

Rubin, A., Chen, E. & Ratner, D., 2015. Basal-Cell Carcinoma. *The New England Journal of Medicine,* 373(11), pp. 2262-2269.

Salimi, A. & Soleymani, S., 2018. Transfollicular Drug Delivery Systems. *Jundishapur Journal of Natural Pharmaceutical Products,* 13(3).

Sarrigiannidis, S. et al., 2021. A tough act to follow: collagen hydrogel modifications to improve mechanical and growth factor loading capabilities. *Materials Today Bio,* 10(100098).

Sciences, N. -. F. L., 2022. *Zeta Potential Measurements.* [Online]
Available at: https://nanocomposix.com/pages/zeta-potential-measurements
[Accessed 28 07 2022].

Scientific, T., n.d. *TEM Imaging - Transmition Electron Microscopy.* [Online]
Available at: https://www.thermofisher.com/pt/en/home/electron-microscopy/products/transmission-electron-microscopes.html
[Accessed 16 september 2022].

Stetefeld, J., McKenna, S. & Patel, T., 2016. Dynamic light scattering: a practical guide and applications in biomedical sciences. *Biophysical reviews,* Volume 8, p. 409–427.

Stummer, W. et al., 1998. Intraoperative Detection of Malignant Gliomas by 5-Aminolevulinic Acid-induced Porphyrin Fluorescence. *Neurosurgery,* 42(3), pp. 518-527.

Thunshelle, C., Yin, R., Chen, Q. & Hamblin, M., 2016. Current Advances in 5-Aminolevulinic Acid Mediated Photodynamic Therapy. *Laser Therapy,* 5(3), pp. 179-190.

Tolosa, L., Donato, M. & Gómez-Lechón, M., 2014. General Cytotoxicity Assessment by Means of the MTT Assay. In: *Protocols in In Vitro Hepatocyte Research.* Chapter 26: s.n., pp. 333-348.

Traylor, J. et al., 2021. Molecular and Metabolic Mechanisms Underlying Selective 5-Aminolevulinic Acid-Induced Fluorescence in Gliomas. *Cancers,* 13(3).

Venus, M., Waterman, J. & McNab, I., 2010. Basic physiology of the skin. *Surgery (Oxford),* 28(10), pp. 469-472.

Verma, A., Jain, A., Hurkat, P. & Jain, S., 2016. Transfollicular drug delivery: current perspectives. *Dove Press - Research and Reports in Transdermal Drug Delivery,* 2016(5), pp. 1-17.

Vijver, M., Zhai, Y., Wang, Z. & Peijnenburg, W., 2018. Emerging investigator series: the dynamics of particle size distributions need to be accounted for in bioavailability modelling of nanoparticles. *The Royal Society of Chemistry - Environmental Science: Nano,* Volume 5, pp. 2473-2481.

Wang, W., Narain, R. & Zeng, H., 2020. Hydrogels. In: *Polymer Science and Nanotechnology - Fundamentals and Applications.* s.l.:Elsevier, pp. 203-244.

Wu, J., 2021. The Enhanced Permeability and Retention (EPR) Effect: The Significance of the Concept and Methods to Enhance Its Application. *Journal of Personalized Medicine,* 11(8), pp. 771-779.

Yamamoto, Y. et al., 2001. Long-circulating poly(ethylene glycol)–poly(D,L-lactide) block copolymer micelles with modulated surface charge. *Journal of Controlled Release,* 77(1-2), pp. 27-38.

Yuan, Y. et al., 2012. Surface charge switchable nanoparticles based on zwitterionic polymer for enhanced drug delivery to tumor.. *Advanced materials,* 24(40), pp. 5476-5480.

Yun, Y. et al., 2018. Artificial skin models for animal-free testing. *Journal of Pharmaceutical Investigation,* Volume 48, pp. 215-223.

Zacheo, A. et al., 2020. Lipid-Based Nanovesicles for Simultaneous Intracellular Delivery of Hydrophobic, Hydrophilic, and Amphiphilic Species. *Frontier in Bioengeneering and Biotechnology,* 8(690).

Zhang, Z. et al., 2016. 5-Aminolevulinic acid loaded ethosomal vesicles with high entrapment efficiency for in vitro topical transdermal delivery and photodynamic therapy of hypertrophic scars. *Royal Society of Chemistry - Nanoscale,* 8(46), pp. 19270-19279.

8. Appendices

Appendix A – EE% found in the literature comparing to EE% obtained

Article	EE% in the author's article	Feeding concentration used	EE% correspondent from the present work	Nanoparticle's materials	Method used
(Zhang, et al., 2016)	~51%	15 mM	10%	Phosphatidylcholine	pH gradient active loading
(Lin, et al., 2016)	15-16%	5mg/mL	< 10%	DPPC and cholesterol	Film hydration method
(Liy, et al., 2021)	43%	Ratio of 1:2 ALA to particles	24%	DOPC, DOPE, SM and CH	Film hydration method
(Luan, et al., 2021)	31,5%	18% (w/w)	42%	DSPC, DSPE-mPEG2000, and cholesterol	Ammonium sulfate gradient technique
(Bragagni, et al., 2015)	75%	20 mg/mL	< 10%	Cholesterol and sorbitan monostearate	Film hydration method
	81%	20 mg/mL	< 10%	Cholesterol and sorbitan monostearate	Reverse phase evaporation

Appendix B – Upper row: cells seeded in medium with a) 0.25% TYP and b) 0.25% SYM. Lower row: cell seeded in medium with c) 0.25% TYP + 0.18% AG and d) 0.25% SYM + 0.18% AG

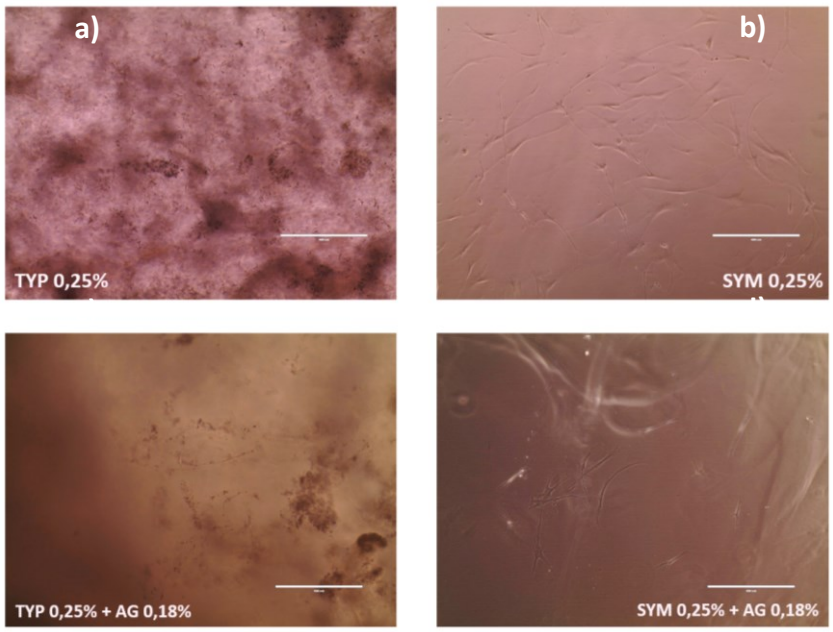

The upper images (a-b) correspond to the studies done to compare two type I collagen samples from different origins: SYMATESE bovine collagen (SYM), used previously in (Quarta, et al., 2021) and proven to have good biocompatibility, and Tilapia collagen (TYP). Basal carcinoma cells were seeded in culture medium, and each collagen type was added, making a final concentration of 0.25%. After 5 days of incubation, the SYM collagen is much more transparent, facilitating the cells' visualization. In the SYM samples, cells grow healthy, while in TYP, the number of visible cells is lower. Since both collagen hydrogels are very soft and liquid, there is the possibility that the material is not supporting cell growth, so the option of adding agarose was considered.

The images c) and d) correspond to the tests done to study the addition of agarose to the collagen hydrogel. Basal carcinoma cells were seeded in the hydrogel with culture media, the final concentration of each collagen was 0.25% and agarose 0.18%. After 3 days of incubation, it is possible to observe healthy cells in the SYM samples, whereas fewer cells were found in TYP samples. Relatively to the mechanical properties, adding agarose was beneficial since it made the hydrogel stiffer.

Although some deductions about the transparency of the materials could be taken, there was not enough data to reach robust conclusions. However, it was possible to conclude that adding agarose was beneficial since the mechanical properties of the hydrogel were significantly better.